The role of electronic structure on Li-ordering and chemical strain in the fast charging Wadsley-Roth phase PNb_9O_{25}

Muna Saber,[†] Molleigh B. Preefer,[‡] Sanjeev K. Kolli,[¶] William Zhang,[§] Geneva Laurita,[‖] Bruce Dunn,[⊥] Ram Seshadri,[¶,§] and Anton Van der Ven[*,¶]

†*Department of Chemical Engineering, University of California, Santa Barbara, Santa Barbara, California 93106, USA*

‡*SLAC National Accelerator Laboratory, Menlo Park, California 95025, USA*

¶*Materials Department, University of California, Santa Barbara, Santa Barbara, California 93106, USA*

§*Department of Chemistry and Biochemistry, University of California, Santa Barbara, Santa Barbara, California 93106, USA*

‖*Department of Chemistry and Biochemistry, Bates College, Lewiston, Maine 04240, USA*

⊥*Department of Materials Science and Engineering, University of California Los Angeles, Los Angeles, California 90095, USA*

E-mail: avdv@ucsb.edu

Abstract

Wadsley-Roth crystallographic shear phases are a family of transition metal oxides that show tremendous promise as electrode materials in Li-ion batteries. Despite their ability to intercalate lithium at high rates, little is known about their structural, thermodynamic and electronic properties as a function of Li concentration. In this study, we use first-principles statistical mechanics methods to explore the lithium site preference, lithiation strain and electronic structure of PNb_9O_{25}, a Wadsley-Roth phase that has been shown to reversibly cycle at a rate of 60C and that can accommodate more than one Li per Nb. We find that Li ions can occupy five symmetrically distinct interstitial sites within the PNb_9O_{25} crystal structure, three being pyramidal sites coordinated by five oxygen and two being window sites with square planar oxygen coordination. The insertion of Li into PNb_9O_{25} leads to a complex site filling sequence, with pyramidal sites preferred at low Li concentrations followed by the filling of window sites at higher Li concentrations. Our findings are aided by neutron diffraction where pyramidal sites are found to be filled at low compositions. The order in which sites are filled is strongly influenced by the chemical strain due to Li insertion. The strain arises from the delocalization of donated electrons over the d orbitals of the structure's edge-sharing niobium, which leads to a tetragonal distortion along the c-axis, thereby making vertical window sites favorable for Li occupancy at intermediate to high Li concentrations. Given the crystallographic similarities among different shear phases, we expect that the results of this study will also shed light on the electrochemical properties of other Wadsley-Roth chemistries.

Introduction

Secondary lithium-ion batteries have become a standard for portable electronics and electric vehicles due to their reliability, high cycle lives, and high efficiencies.[1] Despite their widespread use, Li-ion batteries continue to face challenges in high-power applications, where they have a propensity for thermal runaway reactions due to the formation of lithium dendrites on the anode during fast charging.[2–5] The Li dendrites can pierce the separator and lead to direct contact between the anode and the cathode, thereby increasing explosion risks. These safety concerns

put constraints on the charging times of Li-ion batteries, which limits their use in mobile applications, including electric and hybrid electric vehicles. There is, therefore, a tremendous interest to identify new anode chemistries that are able to rapidly intercalate large quantities of Li and at a slightly higher voltage than the voltage window of graphite based anodes.

The Wadsley-Roth crystallographic shear phases have received much attention in recent years due to their ability to intercalate Li at exceptionally high rates[6] and at voltages that make them viable anode materials. The early studies of lithium insertion into 14 different Wadsley-Roth chemistries by Cava *et al.*[7] demonstrated their ability to accommodate multielectron reduction and oxidation, thereby enabling higher energy densities when compared to intercalation compounds that exchange only one electron per redox center. More recent studies of the electrochemical properties of the Wadsley-Roth chemistries, including VNb_9O_{25},[8,9] $TiNb_2O_7$,[10–13] $Ti_2Nb_{10}O_{29}$,[14,15] $Nb_{12}O_{29}$,[16,17] $Nb_{12}WO_{33}$,[18,19] $Nb_{14}W_3O_{44}$,[20,21] $Nb_{16}W_5O_{55}$,[22] H-Nb_2O_5,[23,24] and T-Nb_2O_5,[25–27] have further confirmed their high capacities and high rate capabilities.

Despite their favorable electrochemical properties, very little is known about the crystallographic changes, electronic structure, and lithium ordering tendencies of Wadsley-Roth phases as a function of Li concentration. Here we report on a combined first-principles and experimental study of the structural and electrochemical properties of the PNb_9O_{25} Wadsley-Roth phase. First studied as an electrode material for Li-ion batteries by Patoux et. al.[8], recent cycling data has shown that PNb_9O_{25} can reversibly cycle for over 500 cycles at a rate of 2C, which corresponds to a thirty minute charge or discharge when tested in a half-cell against lithium.[9] These half-cells were able to maintain a gravimetric capacity of 190 $mAhg^{-1}$. PNb_9O_{25} has also been shown to reversibly cycle up to rates of 60C, though with lower capacities and Coloumbic efficiencies. The insertion of Li into PNb_9O_{25} activates not only the $Nb^{5+/4+}$ redox couple, but also the $Nb^{4+/3+}$ couple.[8,9] A Li:Nb ratio above 1 can, therefore, be achieved, which is greater than the Li to transition metal ratio of 1 that limits the capacity of most other transition metal oxide intercalation compounds. The open structure of PNb_9O_{25} allows for rapid lithium diffusion while operating in a potential window between 2V and 1V and accommodates approximately 11.5 Li when cycled

at a C/20 rate against Li. The higher operating voltage window of PNb_9O_{25} makes it possible to discharge at higher current densities than graphite based anodes that operate at an average potential of 0.1V.[28]

Our systematic study of the electrochemical properties of PNb_9O_{25} as a function of Li concentration reveals a complex site filling sequence that is strongly influenced by the chemical strain induced by changes in the electronic structure that accompany Li insertion. PNb_9O_{25} can host Li in three pyramidal sites and two window sites. The pyramidal sites are filled first, but are then slightly depopulated in favor of window sites. We identify a favorable Li ordering motif over the vertical window sites that forms a persistent backbone at intermediate to high Li concentrations, with the remaining sites accommodating Li through a solid solution. We find that the ordered motif becomes stable after the host undergoes a tetragonal strain due to the delocalization of donated electrons over the d orbitals of edge-sharing Nb cations. Our results show a strong coupling between changes in electronic structure and variations in structural and chemical properties as a function of Li concentration.

Methods

First-principles statistical mechanics calculations

Density Functional Theory (DFT) calculations were performed with the Vienna Ab initio Simulation package (VASP)[29–32] and were used to predict the energies of different lithium-vacancy orderings in $Li_xPNb_9O_{25}$. The generalized gradient approximation (GGA) as formulated by Perdew, Burke, and Ernzerhoff (PBE)[33] was used. The SCAN meta-GGA[34,35] functional was also used to assess the sensitivity of the predictions to the exchange-correlation approximation. This analysis can be found in the Supplementary Information (Figure S1). The interactions between the valence and core electrons was treated with the projector augmented wave (PAW) theory[36,37] and a plane wave energy cutoff of 550eV was used. A fully automatic k-point mesh setting corresponding to a $2\times2\times7$ Monkhorst-Pack grid was used for the primitive unit cell. Crystal structures and charge

densities were visualized with VESTA.[38] A charge density isosurface of 0.004 $Å^{-3}$ was used for all calculations.

The electrochemical properties associated with Li insertion into PNb_9O_{25} were studied with a cluster expansion approach in combination with Monte Carlo simulations using the CASM code.[39–42] The PNb_9O_{25} unit cell contains 20 stable lithium sites. Without taking symmetry into account, there are over 1 million different Li-vacancy orderings over the sites of the primitive unit cell of PNb_9O_{25}. This number of Li-vacancy orderings increases considerably within supercells of PNb_9O_{25}. To sample important Li-vacancy configurations, we used an iterative approach whereby the energies of an initial sampling of Li-vacancy configurations were used to parameterize a cluster expansion, which was subsequently used to identify low-energy Li-vacancy configurations. The cluster expansion fit was iteratively improved with every batch of new low-energy orderings. Cluster expansion Hamiltonians were used in Monte Carlo simulations to predict finite temperature thermodynamic properties such as the voltage curve.[41,43–53]

Experimental Methods

Materials preparation

PNb_9O_{25} was prepared using traditional solid-state methods. Stoichiometric ratios of $(NH_4)_3PO_4$ (Sigma Aldrich, 98%) and Nb_2O_5 (Materion, 99.95%) were ground together using an agate mortar and pestle for 20 minutes. The resulting powder mixture was pressed into a 13 mm pellet under 2.5 tons of force with a total mass of 1.5 g. The pellet was placed into an alumina crucible on a bed of the powder mixture and annealed at 623 K in air. After 20 hours, the furnace was adjusted to 1523 K, and the pellet annealed for another 18 hours. The pellet was slow-cooled in the atmosphere of the furnace and reground in a mortar and pestle for use. Additional descriptions can be found in previous work.[8,9]

Electrochemical characterization

The material was ball-milled in a 5 mL stainless steel grinding vial with SuperP (TIMCAL). A slurry was prepared by speedmixing a polyvinylidene fluoride binder (Kynar, Arkema) with N-methyl-2-pyrrolidone at 2000 rpm for 10 minutes until dissolved. Then the active material and SuperP mixture was added to the mixture and speedmixed at 2000 rpm for 10 minutes until a uniform suspension was formed. The resulting viscosity was equivalent to honey, and the ratio of active material:carbon:binder was 72:18:10 by weight. The mixture was cast onto Cu foil using a doctor blade set to 150 μm and dried under vacuum at 90 deg C. 10 mm diameter discs were punched, and a typical mass loading is 1.5 mg/cm ^{2}. 2032 coin cells were assembled in an Ar-filled glovebox ($H_2O < 0.1$ ppm, $O_2 < 0.1$ ppm) using a polypropylene separator (Celgard 2500) and flooded with 1 M $LiPF_6$ in ethylene carbonate/dimethyl carbonate (EC/DMC, Sigma Aldrich). Polished Li discs were used as a combined counter and reference electrode. Galvanostatic intermittent titration technique (GITT) was performed using a VMP3 potentiostat (Bio-logic) at a rate of C/40 with a 30-minute current step and 90-minute rest periods between a voltage window of 1 – 3V. To be consistent with prior work on $Li_xPNb_9O_{25}$,[9] we calculate the rate based on 12 Li ions inserted into the formula PNb_9O_{25}, such that C/40 = 12Q/40 = 254 mAh g^{-1} /40 h = 6.35 mA g^{-1}. We point out, however, that the maximum theoretical capacity based on crystallographically available Li sites is 20 per PNb_9O_{25} formula unit.

Neutron scattering and refinements

In order to produce ex-situ material at differing states of lithiation, PNb_9O_{25} was electrochemically cycled as loose powder that was mechanically ball milled with SuperP (TIMCAL) in a 5 mL stainless steel can for 30 minutes (80$\%$ active material by weight). Approximately 200 mg of the mixture was carefully loaded onto a stainless steel plunger of a swagelok cell with a 1.5 inch diameter. The powder was compacted with two glass fiber separators (Whatman GF/D) cut to size and compressed with another plunger. The cells were assembled in an Ar-filled glovebox ($H_2O < 0.1$ ppm, $O_2 < 0.1$ ppm) using enriched ^{7}Li as the counter electrode (Sigma Aldrich) and

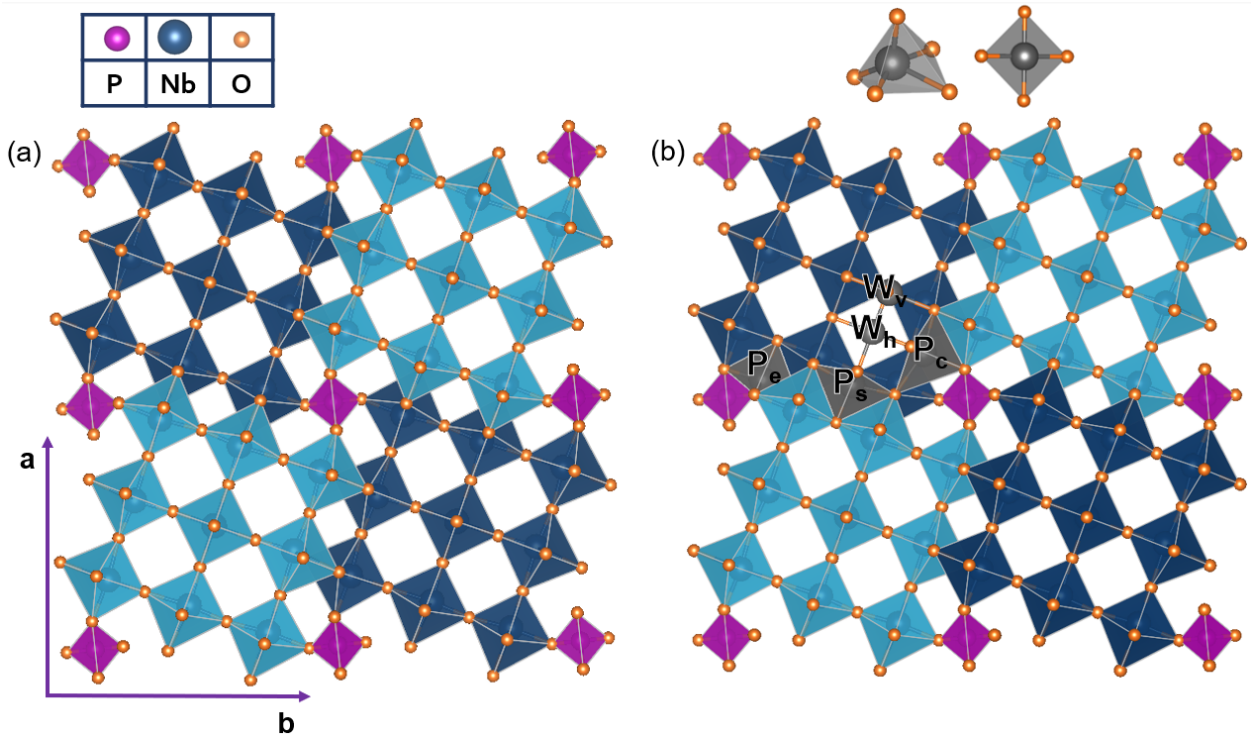

Figure 1: (a) The crystal structure of PNb_9O_{25} as viewed down the c axis. The octahedra correspond to NbO_6, the tetrahedra correspond to PO_4. (b) The pyramidal and square polyhedra show one example of each symmetrically distinct lithium site.

enriched $^{7}LiPF_6$ (Sigma Aldrich) made into a 1 M electrolyte solution in 1:1 v/v EC/DMC (Sigma Aldrich). The cells were cycled at a rate of C/80 to ensure expected lithiation in the bulk, loose powder format. The first cell was cycled to 1.695 V (OCV = 3.1 V, 1.5 Li inserted), and the second cell was cycled to 1.635 V (OCV = 3.2 V, 4.3 Li inserted). The Galvanostatic discharge profiles are provided in the Supplementary information (Figure S2). The cells were deconstructed in the Ar-filled glovebox, and the cycled materials were scraped off of the stainless steel plunger. The powders were washed three times in dimethyl carbonate and dried under vacuum. Once dry, they were loaded into glass capillaries as provided by the mail-in program at NOMAD (BL-1B, Spallation Neutron Source, Oak Ridge National Laboratory), where the time-of-flight data was collected at room temperature (Figure S3). Rietveld refinements on the diffraction data were done using GSAS-II using both banks 4 and 5.[54] The non-lithiated structure was refined using the previously-reported structure solution for PNb_9O_{25} (space group I4/m, 87).[55] Both atomic positions and atomic displacement parameters were allowed to refine. The lithiated structures were refined by placing Li onto the expected Wyckoff positions within the parent structure based on the predicted structures from the DFT calculations. The structure was first refined against the original PNb_9O_{25} structure without Li. Then, Li was systematically placed onto each of the 5 identified sites, separately. Position (except special positions), isotropic atomic displacement parameters, and lattice parameters were allowed to refine. All occupancies, including Li, were fixed to the nominal stoichiometry as derived from the electrochemical experiments. The unphysical results were separated from the physical results to identify the plausible experimental structures. For all patterns, backgrounds were initially fit graphically with a 36-term polynomial to account for the amorphous nature of the carbon additive and left fixed for the remainder of the refinements. Visualizations of the crystal structures from the resulting cif files were done using VESTA.[38] Partial pair distribution functions can be found in the Supplementary information (Figure S4) and were calculated using the PDFgui program.[56]

Results

Lithium site preferences and lithium ordering

The PNb_9O_{25} compound is a member of the Wadsley-Roth family of crystallographic shear phases.[18,57–59] The PNb_9O_{25} unit cell, shown in Figure 1(a), consists of $3 \times 3 \times \infty$ blocks of corner-sharing NbO_6 octahedra that are connected to each other by edge sharing NbO_6 octahedra along each block periphery. The blocks are offset along the a and b lattice vectors, allowing for a tetrahedral PO_4 site at the block corners. There are two symmetrically equivalent tetrahedral sites per unit cell, one above the other along the c axis, that can be occupied by P. In experimentally prepared samples, P fills these sites with equal probability, leading to a partial occupancy of 0.5. In all our calculations, we picked one of the two sites, and thereby work with a model that has an increased degree of order and hence a lower symmetry. Furthermore, the experimentally refined structure of PNb_9O_{25} has the Nb at the center of the block distributed over two off-centered positions with partial occupancies of 0.5. These off-centered positions cannot be simultaneously occupied by two Nb. In all our calculations, the position of the Nb at the center of the block was initialized at the geometric average of the off-centered positions.

We have identified five symmetrically distinct candidate lithium sites in PNb_9O_{25}. An example of each type of site is shown in Figure 1(b). The P_e, P_c and P_s sites are pyramidally coordinated by oxygen and reside along the block periphery. Each P_e site shares an edge with a PO_4 tetrahedron while each P_c site shares a corner with a PO_4 tetrahedron. The P_s sites are located in the middle of the block periphery and are coordinated by six NbO_6 octahedra. Li can also reside in two symmetrically distinct window sites: the vertical W_v sites and the horizontal W_h sites. These sites reside in the interior of the $3 \times 3 \times \infty$ blocks of corner-sharing NbO_6 octahedra and are each coordinated by a planar square of oxygen ions. Each of the five symmetrically distinct Li sites have a multiplicity of four per unit cell. The stability of pyramidal and window sites in PNb_9O_{25} is consistent with past neutron diffraction and first-principles studies by Catti et al[60–62] and Morris et al[22,63] of other Wadsley-Roth phases.

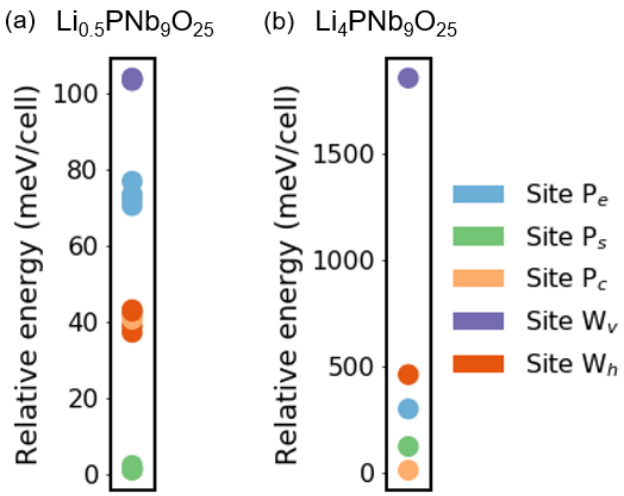

Figure 2: (a) Energies per unit cell of different Li-vacancy orderings in $Li_xPNb_9O_{25}$ at x=0.5. The energies were calculated with DFT-PBE in a super cell containing 2 unit cells stacked along the c-axis. The lowest energy configuration was chosen as the reference (i.e. the zero of the energy scale). P_e, P_s, and P_c refer to different pyramidally coordinated Li sites (b) Energies per unit cell of $Li_xPNb_9O_{25}$ at x=4, in which all symmetrically equivalent sites of a particular Li site are completely filled.

We first investigated Li site preferences at very dilute Li concentrations. All symmetrically distinct arrangements of a single Li within a super cell containing two units of PNb_9O_{25} stacked along the c-axis were enumerated. This corresponds to a Li concentration of x=0.5 in $Li_xPNb_9O_{25}$. Figure 2(a) shows their energies as calculated with DFT-PBE. At this very dilute concentration, Li prefers the pyramidal P_s sites. The least favored site is the vertical window site W_v. The Li site preference changes upon the addition of more Li. This is evident in Figure 2(b), which shows the energy at x=4 in which all four symmetrically equivalent sites of each type of Li site are filled. At this concentration, the P_c sites are preferred over the P_s sites. Note the large change in energy scale in Figure 2(b) compared to that in Figure 2(a).

We further explored Li site preferences and ordering tendencies over the whole composition range $0 < x < 20$ in $Li_xPNb_9O_{25}$ by calculating the formation energies of 4298 Li-vacancy orderings over all five candidate Li-sites within differently sized super cells with DFT-PBE. The calculated formation energies are shown in Figure 3. The majority of these orderings were enumerated with CASM[39,40,42,64] using the cluster expansion in an iterative approach to identify low-energy

Li-vacancy orderings within $Li_xPNb_9O_{25}$. To highlight changes in site preference as a function of Li concentration, we have color-coded configurations based on their site occupancies. The three formation energy plots and the accompanying schematics show which site types are filled in the lowest energy orderings in three separate composition intervals.

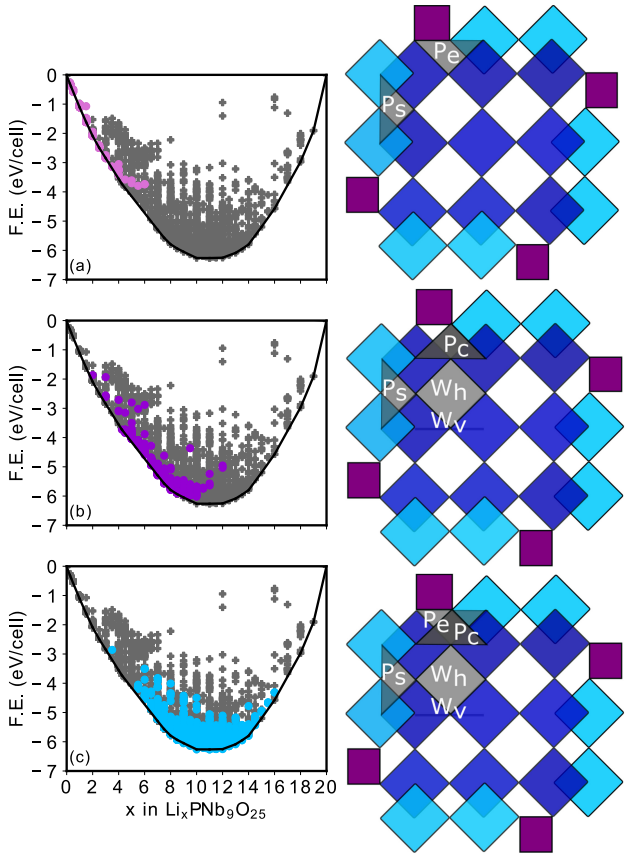

Figure 3: Calculated formation energies of 4298 Li-vacancy orderings within $Li_xPNb_9O_{25}$. (a) Configurations in which Li only occupies the P_s and/or P_e sites are highlighted. (b) Configurations with some degree of Li occupancy of the P_c sites as well as W_h and/or W_v sites are highlighted. (c) Configurations with all P_c sites filled by Li and a partial filling of P_s, W_h and/or W_v sites by Li are highlighted.

At low compositions ($0 < x < 3$), the low energy Li-vacancy orderings have Li occupying the P_s and/or P_e sites. The energies of these configurations are shown in pink in Figure 3(a). A site preference inversion occurs at x=4 where the lowest energy Li-vacancy ordering has three Li per unit cell occupying the P_c site and one Li per unit cell occupying the P_e site. Beyond x=4, the P_s and P_e sites are no longer preferred and all ground states and low energy orderings have completely filled P_c sites. Furthermore, both the horizontal and vertical window sites, W_h

and W_v, which are not favored at dilute Li concentrations, start filling as more Li is added. The energies of orderings with P_c, W_h and W_v partially or fully filled are shown in purple in Figure 3(b). As the Li concentration increases further, the P_s sites start filling again in the low energy orderings. The energies of configurations in which all the P_c sites are filled and where the W_h, W_v and P_s sites are fully or partially occupied are shown in light blue in Figure 3(c).

An intriguing feature about the ground states and a large number of low energy orderings in the interval $7 < x < 14$ is that almost all share a common Li-vacancy ordering over the W_v vertical window sites. This ordering leads to a doubling of the unit cell along the c-axis and can be described as an interweaved pattern with pairs of occupied W_v sites alternating their orientation by 90^o upon moving along the c-axis as shown in Figure 4. The composition at which this ordering can set in is x=6, with all four P_c sites and two of the four W_v sites filled per unit cell. Additional Li is then accommodated by the gradual filling of the horizontal W_h sites followed by the P_s sites. Schematics of the ground state orderings can be found in the Supplementary Information (Figures S5-9).

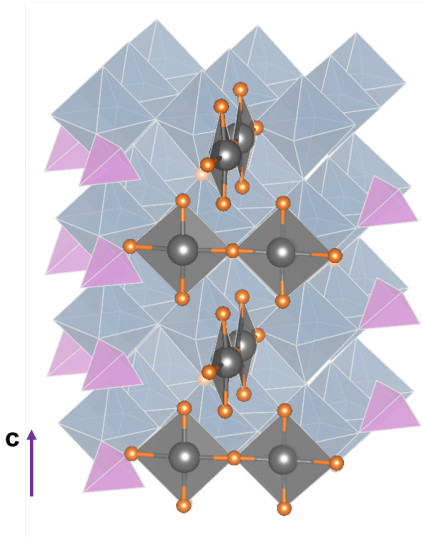

Figure 4: The interweaved Li-vacancy ordering over the W_v sites that forms the backbone of all ground states as predicted with DFT-PBE between x=7 and x=14. The ordering consists of pairs of occupied W_v sites that alter their orientation by 90^o upon moving along the c axis.

The convex hull connecting the formation energies of the ground state orderings can be used to calculate the voltage profile of $Li_xPNb_9O_{25}$ relative to a pure Li anode at zero kelvin. The

slopes along the convex hull are linearly related to the Li chemical potential μ_{Li}, which in turn determines the voltage according to the Nernst equation.[43] Figure 5 shows the zero kelvin voltage curve of $Li_xPNb_9O_{25}$. Each step corresponds to a stable Li-vacancy ordering over the sites of $Li_xPNb_9O_{25}$, while the plateaus represent equilibrium voltages at which one stable Li-vacancy ordering transitions to another through a two-phase reaction. The plot also summarizes the site preference in the ground state orderings as a function of Li concentration, clearly showing a dramatic shift in site preference between x=3 and $x \approx 4$ through a two-phase reaction. The interweaved ordering of Figure 4 sets in around x=7 and is present in most subsequent ground states up to x =14.

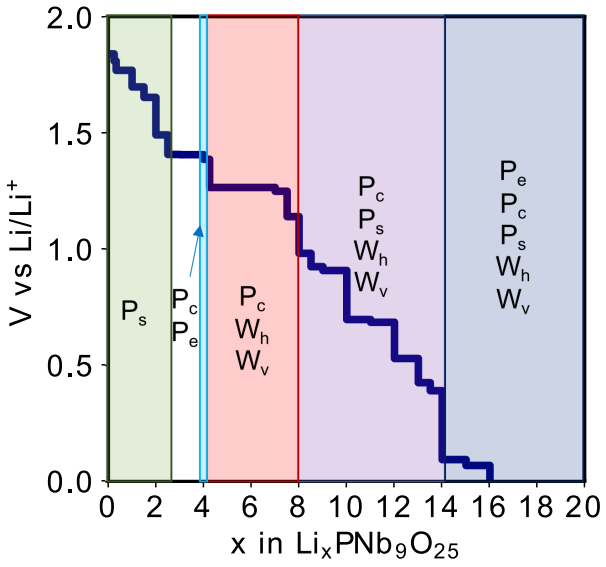

Figure 5: Calculated voltage curve of $Li_xPNb_9O_{25}$ at zero kelvin. Each step corresponds to a ground state Li-vacancy ordering and each plateau corresponds to the voltage of a two-phase reaction. Also shown are the occupied sites in the ground states as a function of Li concentration x.

Electrochemical properties at Finite Temperatures

We next explored the effect of temperature and thermal excitations on the electrochemical properties of $Li_xPNb_9O_{25}$ using statistical mechanics approaches that rely on the cluster expansion method and Monte Carlo simulations. The inclusion of the effects of temperature facilitates com-

parisons to experimentally measured electrochemical properties. We only considered configurational degrees of freedom associated with the many possible ways of arranging Li and vacancies over the sites of $Li_xPNb_9O_{25}$. The cluster expansion approach was used to extrapolate the DFT-PBE formation energies of Figure 3 within Monte Carlo simulations. More details about this approach can be found elsewhere.[41,43]

Two separate cluster expansions were trained using the formation energies calculated with DFT-PBE. The first cluster expansion was restricted to the P_s and P_e sites and was used to calculate electrochemical properties at low Li concentrations, where these sites are preferred. A second cluster expansion was constructed that explicitly treated Li occupancy on the W_h, W_v and P_s sites while keeping the P_c sites filled. This cluster expansion was used to predict finite temperature properties between x=4 and x=16, where as predicted by the DFT formation energies of the previous section, all low energy configurations (with the exception of the ground state at x=4) have completely filled P_c sites and varying degrees of Li occupancy over the W_h, W_v and P_s sites. Details about the cluster expansion fits can be found in the Supplementary Information (Figures S10-11).

Figure 6(a) shows the voltage curve (dark blue) of $Li_xPNb_9O_{25}$ as calculated with Monte Carlo simulations at 300 K. The Monte Carlo simulations were applied to the cluster expansions to calculate the concentration dependence of the Li chemical potential, which was in turn substituted into the Nernst equation[43] to obtain the voltage curve. A $10\times10\times20$ super cell of the PNb_9O_{25} primitive cell was used. Most of the steps and plateaus that are present in the zero kelvin voltage curve of Figure 5 have been smoothed out due to contributions from configurational entropy at 300 K. A sloping voltage profile is generally a sign of a disordered solid solution. Also shown is an experimental voltage curve (purple) of $Li_xPNb_9O_{25}$ measured with GITT. While the calculated voltage curve has a similar shape, it is lower than the experimental curve. It is common that approximations to density functional theory, such as the PBE approximation used in this work, systematically under predicts voltages.[43]

Both the calculated and experimental voltage curves exhibit a plateau signifying a two-phase

reaction between x=2 and x=4. The existence of a two-phase reaction between x=2 and x=4 was first reported by Patoux et al[8] and was recently confirmed by others[9,65] using in-situ diffraction. The Monte Carlo simulations indicate that the two-phase reaction arises from a change in site preference. This is evident in Figure 6(b), which plots the average concentrations of each type of Li site as calculated with the Monte Carlo simulations. Below x=2, the Li predominantly occupies the P_s sites (green), with some occupancy on the P_e sites (blue). Upon crossing the two-phase region between x=2 and x=4, the site preference switches abruptly, with four Li per unit cell occupying the P_c sites (light orange) and none occupying P_s and P_e. The abrupt increase in the number of occupied P_c sites at x=4 is an artefact of our cluster expansion model. Our zero kelvin DFT-PBE calculations predict that the ground state at x=4 has only 3 Li in P_c and a fourth in P_e and we therefore expect some P_e occupancy at finite temperature.

A second plateau is evident in the calculated voltage curve that is not present in the experimental voltage curve between x=5 and x=7. It is possible that there is more structural disorder in the experimental samples (e.g. due to partial occupancy of the two equivalent P sites) such that the predicted two-phase region between x=5 and 7 gives way to a solid solution. The average site occupancies as calculated with Monte Carlo simulations in Figure 6(b) indicates that passage through the second two-phase region leads to an abrupt increase in the concentration of occupied vertical window sites W_v. This is due to the onset of the interweaved Li-vacancy ordering over half the W_v sites shown in Figure 4. The interweaved ordering remains locked in place until x=14, with additional Li filling the W_h horizontal window sites and then the P_s sites in a continuous and disordered manner. This is a unique example of an intercalation process where Li ions adopt a stable ordered arrangement over a subset of sublattices and a solid solution over the other sublattice sites. While some Li are locked into a well ordered arrangement over the P_c and W_v sites, their disordered arrangement over the W_h and P_s sites leads to a smooth and sloping voltage curve. It is likely that this partial ordering tendency that is restricted to one sublattice will have significant implications for the kinetics of Li diffusion and reversibility of the compound.

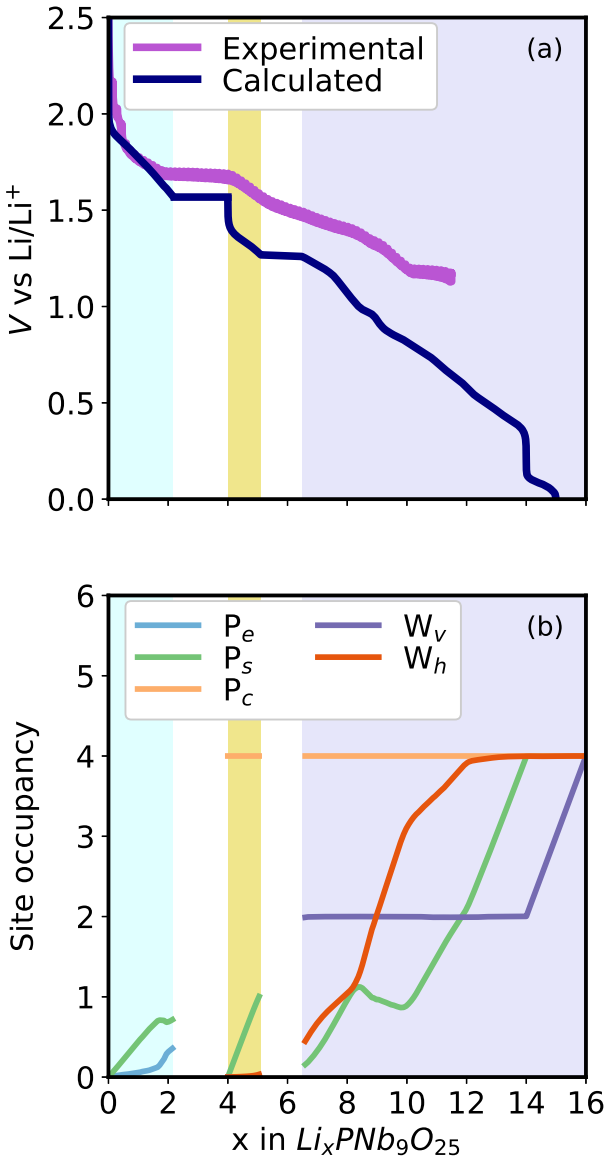

Figure 6: (a) Equilibrium voltage curve at 300K as calculated with grand canonical Monte Carlo simulations applied to cluster expansions of the Li-vacancy energy in PNb_9O_{25}. (b) Calculated site occupancy as a function of Li concentration.

Neutron Diffraction

Our systematic investigation of Li-vacancy orderings in $Li_xPNb_9O_{25}$ with DFT-PBE calculations predicts a change in Li site preference between x=2 and x=4. At dilute concentrations, Li ions prefer the P_s and P_e sites, but they switch their preference to the P_c sites, albeit with a small fraction of Li still in the P_e sites, when the Li concentration x is in the vicinity of 4. The calculations also clearly predict the absence of Li in window sites below x=6. To validate these predictions, we used neutron diffraction to determine site occupancy in $Li_{1.5}PNb_9O_{25}$, a composition before the plateau, and in $Li_{4.3}PNb_9O_{25}$, a composition immediately after the plateau (Figures 7(b-g)).

Extreme care was taken to measure lithiated samples that are representative of the galvanostatic discharge of cast electrodes. Typical open circuit voltages for PNb_9O_{25} as cycled in coin cells range between 3.0 – 3.2 V. The cell that resulted in the insertion of an average of 1.5 Li into PNb_9O_{25} (as determined by the galvanostatic discharge) started with an OCV of 3.1 V. Similarly, the cell that resulted in the insertion of 4.3 Li into PNb_9O_{25} started with an OCV of 3.2 V. The galvanostatic discharge profile of both cells cycled at a rate of C/80, with an average of 200 mg of loose powder (160 mg active material) per cell, mirrored that of the GITT experiment (Figure 7(a)). The large mass loadings are necessary to acquire neutron scattering data, and one giant cell was used to minimize the possibility of combining material across multiple cells that may have lithiated inhomogeneously. The characteristic initial plateau observed at 2 V, corresponding to the insertion of roughly 0.4 Li per formula unit, can be clearly seen in both traces. Therefore, we are confident that the collected Neutron scattering data is an accurate representation of the structures of previous studies[8,9] at the selected states of discharge.

Rietveld refinements were performed on the $Li_{1.5}PNb_9O_{25}$ and $Li_{4.3}PNb_9O_{25}$ samples by considering each of the five Li sites, P_c, P_e, P_s, W_h, W_v. All structures retained the symmetry of the parent compound and could be fit to the I4/m space group. For both $Li_{1.5}PNb_9O_{25}$ and $Li_{4.3}PNb_9O_{25}$, the results from fitting the structure with the two window sites, W_h and W_v, led to unphysical bond lengths (highly distorted Li–O polyhedra and in some cases Nb–O polyhedra). Key parameters from these refinements can be found in Supplemental Tables 1 and 2. Therefore,

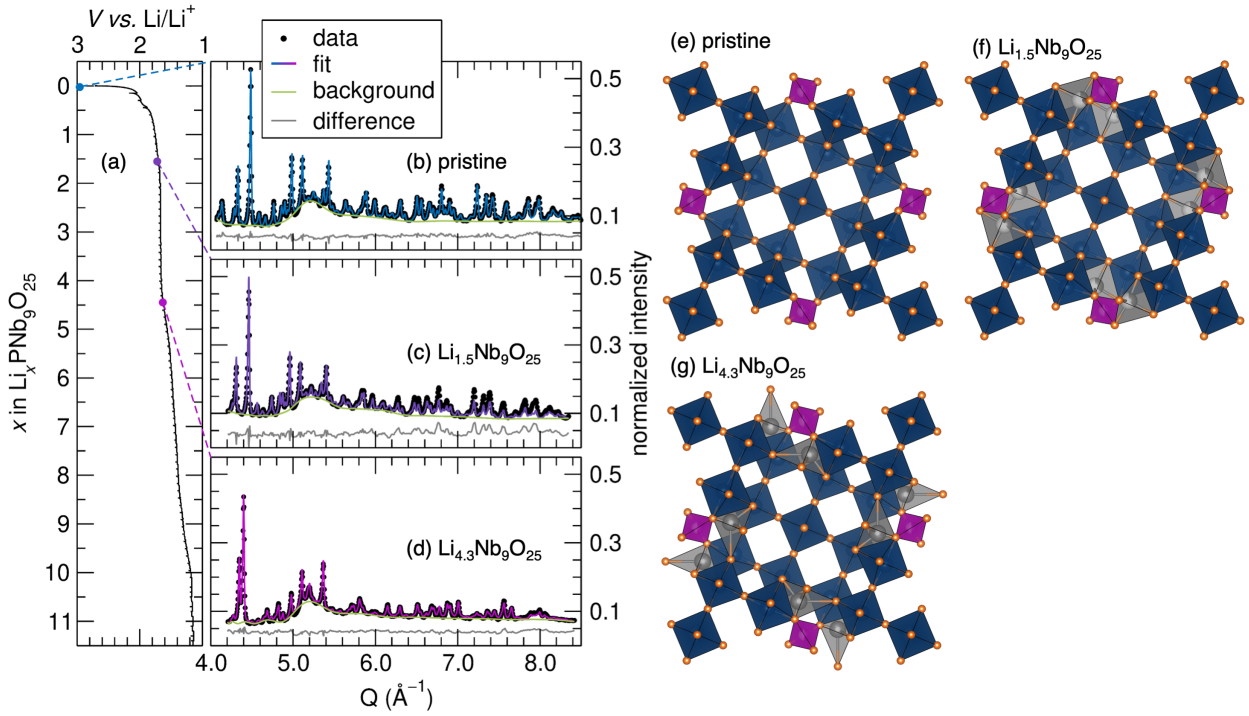

Figure 7: (a) GITT of PNb_9O_{25} between 3 and 1 V (first discharge). Neutron diffraction from NOMAD at the Spallation Neutron Source at Oak Ridge National Lab (bank 5 represented) of (b) pristine PNb_9O_{25} mixed with SuperP, (c) $Li_{1.5}PNb_9O_{25}$ lithiated as loose powder mixed with SuperP, and (d) $Li_{4.3}PNb_9O_{25}$ lithiated as a loose powder mixed with SuperP. The fit and difference curves are a result of Rietveld refinements, and all structures were fit with the I 4/m space group (87). Representations of the crystal structures as determined by the shown Rietveld refinements for (e) the pristine material, (f) $Li_{1.5}PNb_9O_{25}$, and (g) $Li_{4.3}PNb_9O_{25}$. $Li_{1.5}PNb_9O_{25}$ is best described by the configuration with Li in the P_e site, though P_s is also a candidate site. $Li_{4.3}PNb_9O_{25}$ is best described by the configuration with Li in the P_c site, though P_e and P_s are very statistically similar. Further refinements for these alternate configurations can be found in the Supplementary Information (Figures S12-17).

the window sites are deemed as unlikely candidates for Li insertion at these compositions from the experimental data. Among the fits that gave physical results for $Li_{1.5}PNb_9O_{25}$, the refinement for Li in the P_e site yielded the lowest refined Li thermal parameter and lowest R_{wp} (weighted profile residual) values for both banks 4 and 5. Li occupancy in P_s is also a candidate structure, as Li–O bond lengths, thermal parameters, and R_{wp} values are all reasonable, as well. Li in the P_c site yields highly distorted Li–O tetrahedra, pointing to an unlikely solution. Both window sites yielded unphysical values. It is worth noting that while peak position and peak shape are being fit well in the candidate structures, peak intensities, particularly at high Q, are not. This points to some disorder that is not being captured adequately in the structure, together with the already relatively high thermal parameters. This is not surprising given that the fits only take into account one Li site at a time, which are already partially occupied. The structure at x=1.5 likely has combined Li occupancy in the P_e and P_s sites, and possibly in the P_c site. Similarly, the refinements for the P_c, P_s, and P_e sites yielded reasonable fits for $Li_{4.3}PNb_9O_{25}$, suggesting any of these sites are candidates at this composition. Among these three, Li in the P_c site gave the lowest thermal parameters and lowest R_{wp} values for banks 4 and 5. However, all three refinements are statistically similar. Likely all three Li environments can be found in the structure at this composition.

Effect of Lithium Insertion on Strain and Volume

The insertion of Li into an intercalation compound usually results in a change of its volume and unit cell shape, which can lead to electrode fragmentation and fracture, and thereby capacity fade.[66,67] Dimensional changes of an intercalation compound can be measured with symmetry adapted strain order parameters.[41,68,69] A convenient set of symmetry adapted strain order pa-

rameters for a tetragonal crystal such as PNb_9O_{25} takes the form[68]

$$\begin{pmatrix} e_1 \\ e_2 \\ e_3 \\ e_4 \\ e_5 \\ e_6 \end{pmatrix} = \begin{pmatrix} \frac{(E_{xx}+E_{yy}+E_{zz})}{\sqrt{3}} \\ \frac{(E_{xx}-E_{yy})}{\sqrt{2}} \\ \frac{(2E_{zz}-E_{xx}-E_{yy})}{\sqrt{6}} \\ \sqrt{2}E_{yz} \\ \sqrt{2}E_{xz} \\ \sqrt{2}E_{xy} \end{pmatrix} \quad (1)$$

where E_{xx}, etc. are conventional strains of the $Li_xPNb_9O_{25}$ unit cell relative to the fully relaxed PNb_9O_{25} reference state having tetragonal symmetry with its c axis aligned parallel to the Cartesian $\hat{z}$ axis.

The first strain order parameter, e_1, measures dimensional changes of the unit cell that are symmetry invariant. When using Hencky strains, e_1 becomes equal to the change in the volume of $Li_xPNb_9O_{25}$ relative to that of the PNb_9O_{25} reference volume.[68] Figure 8(a), shows the e_1 strain order parameter for each of the 4298 fully relaxed Li-vacancy orderings of $Li_xPNb_9O_{25}$ considered in this work. Figure 8 clearly shows an overall increase in the volume of the cell upon the insertion of Li. The volume of the lowest energy configurations (darker points) increase monotonically up to x=4, decrease slightly between x=4 and 7, but then increase again beyond x=7. The overall increase in volume is consistent with the in-situ diffraction study of Patoux et al.[8] For example, the calculated volume change at x=10.25 is approximately 7%. This value is in quantitative agreement with the value extracted from in situ XRD,[8] where the volume changed by 7.4% upon the insertion of 10.25 Li. The slight reduction in volume between x=4 and 7, however, is not observed experimentally, with the study of Patoux et al[8] showing instead a slight expansion.

The other strain order parameters are plotted in Supplementary Information (Figure S18). One that varies appreciably with Li concentration is e_3, which is also shown in Figure 8(b). The e_3 strain order parameter filters out tetragonal distortions of the crystal. For $Li_xPNb_9O_{25}$, a positive value of e_3 measures an elongation along the c axis, which is parallel to the block length,

and a uniform contraction perpendicular to the c axis as shown in Figure 9(a). It is a measure of the change in the c/a ratio of a conventional tetragonal unit cell. Figure 8(b) shows that e_3 remains close to zero up to $x \approx 4$, increases over a narrow concentration interval to a value of approximately 7%, and subsequently remains relatively unchanged beyond x=7. While there is a large scatter in e_3 values between x=4 and x=7, outside of this interval the e_3 values are relatively insensitive to the Li-vacancy ordering and are instead largely determined by the average concentration. This implies that the dimensional changes with Li concentration as measured by e_3 are affected by a global property, such as a shift in the Fermi-level, that is more sensitive to the average concentration than to any particular Li-vacancy ordering. It should be noted that the abrupt increase of e_3 around x=7 for the ground state structures (connected by the blue line in Figure 8(b)) coincides with the onset of the interweaved ordering over the W_v vertical window sites (Figure 4). A similar elongation of the blocks coupled with an in-plane constriction perpendicular to the blocks was observed by Patoux et al [8] for $Li_xPNb_9O_{25}$ and by Kocer et al [22,70] in other Wadsley-Roth phases.

The variation of e_3 with Li concentration in the ground states is strongly correlated with changes in the Nb-Nb pair distances of edge sharing NbO_6 octahedra at the periphery of the blocks. Figure 8(c) shows that the average Nb-Nb distances decrease from values that range between 3.4 and 3.5 Å for $x < 4$ to values that average around 3.0 Å above x=7. Below x=4, the edge sharing NbO_6 octahedra of the block peripheries are highly distorted due to the off-centering of the Nb cations that arises from a second-order Jahn-Teller distortion as shown in Figure 9(b). The four coordinating oxygen ions of the vertical window sites form a highly distorted square for $x < 4$, with two sets of oxygen pairs having a larger bond length than the remaining two. The distortions of the edge-sharing NbO_6 octahedra and the vertical window sites are largely absent above x=7 as shown in Figure 9(c). A shortening of the Nb-Nb distance for the edge-sharing NbO_6 octahedra leads to an elongation along the block length (i.e. c axis) and a simultaneous contraction in a plane perpendicular to the block length. These dimensional changes have their origin in modifications to the electronic structure that occurs upon Li insertion, as is described

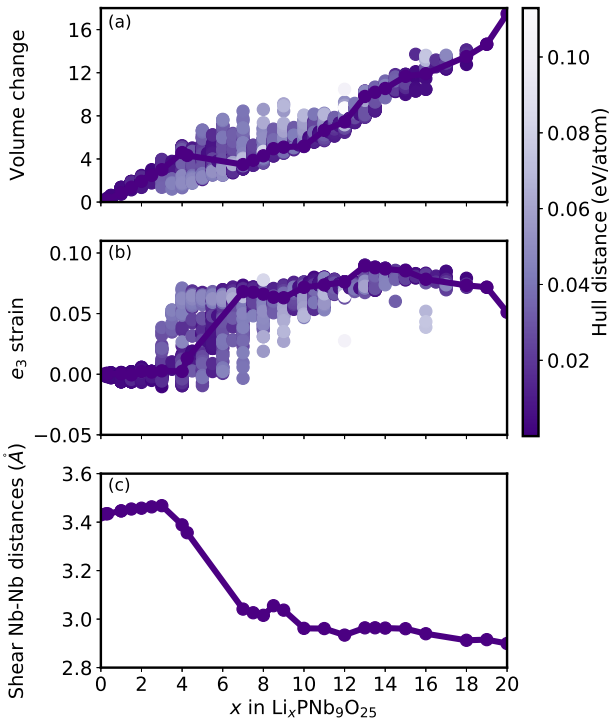

Figure 8: (a) The volume change of $Li_xPNb_9O_{25}$ relative to that of fully relaxed PNb_9O_{25} for each of the 4298 Li-vacancy orderings studied with DFT-PBE. Darker colors, tending towards purple, correspond to orderings with a lower energy, while lighter colors signify orderings with a high energy (measured as the distance from the convex hull). The ground states are connected with a black line. (b) The e_3 strain order parameter for the same 4298 Li-vacancy orderings, which measures an elongation along the c axis (parallel to the block length) and a contraction in the plane perpendicular to the c axis. (c) Bond distances between niobium ions in the edge-sharing octahedra at the perifery of the blocks of the ground state structures.

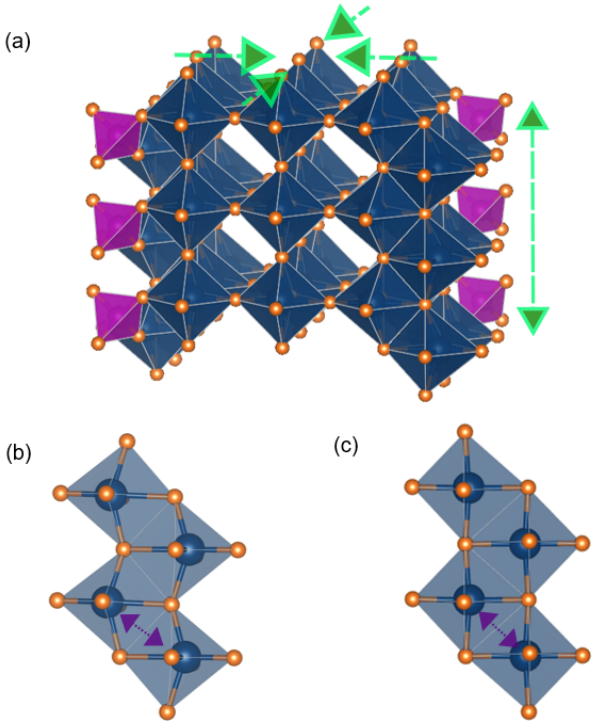

Figure 9: (a) Schematic of the strain measured with the e_3 strain order parameter. An increase in e_3 corresponds to an expansion along the c axis and a constriction in the plane perpendicular to the c axis. (b) Visualization of the edge-sharing niobium octahedra at a low composition, $Li_{0.5}PNb_9O_{25}$. At low Li compositions, Nb^{5+} of the edge-sharing NbO_6 octahedra undergo a second-order Jahn-Teller distortion. (c) At high Li concentrations, the distortions go away and the distance between edge-sharing Nb decreases.

in the next section.

Electronic Structure

The Nb cations of PNb_9O_{25} have a formal oxidation state of 5+. The Nb d levels, when octahedrally coordinated by oxygen, split into three degenerate t_{2g} (d_{xy}, d_{xz}, d_{yz}) levels with lobes that point between oxygen ions and two e_g levels (d_{z^2} and $d_{x^2-y^2}$) with lobes that point towards the oxygen as shown in the Supplementary Information (Figure S19). The degeneracy of the t_{2g} and e_g levels are lifted further when the symmetry of the NbO_6 octahedra are lowered by the surrounding crystal and/or distortions of the octahedra themselves. In PNb_9O_{25}, all the t_{2g} and e_g levels are empty and the compound is an insulator. The e_g levels, which are anti-bonding states that arise from a hybridization between Nb d_{z^2} and $d_{x^2-y^2}$ orbitals and the surrounding oxygen p orbitals, have a higher energy than the t_{2g} levels. When Li atoms are added to PNb_9O_{25}, they will, therefore, donate their electrons to the t_{2g} levels.

Figure 10 shows the charge density of the occupied t_{2g} levels upon the addition of a very dilute concentration of Li. The calculation was performed on a supercell consisting of four PNb_9O_{25} unit cells and one Li ion, constituting a Li concentration of x=0.25. As is evident in Figure 10, the electron donated by the Li atom fills a t_{2g} orbital on a Nb that resides in a corner sharing NbO_6 octahedron at the center of the $3\times3\times\infty$ block. The t_{2g} orbitals in these octahedra are non-bonding and, therefore, highly localized, as is evident in Figure 10.

It is only after the non-bonding t_{2g} orbitals at the centers of the blocks are filled that a further addition of Li leads to a gradual filling of t_{2g} levels on the Nb cations that reside in the edge-sharing NbO_6 octahedra at the periphery of the blocks. This is evident in Figure 11. The charge density of the filled t_{2g} states of $Li_5PNb_9O_{25}$ shown in Figure 11 reveals not only electron density on all the non-bonding t_{2g} levels at the center of the blocks, but also an appreciable density on the Nb in the edge-sharing octahedra. An increase of the Li concentration to x=7 results in a further accumulation of charge on the t_{2g} states of the edge-sharing NbO_6 octahedra as is evident in $Li_7PNb_9O_{25}$. In fact the charge density of $Li_7PNb_9O_{25}$ in Figure 11 suggests the onset of Nb-Nb

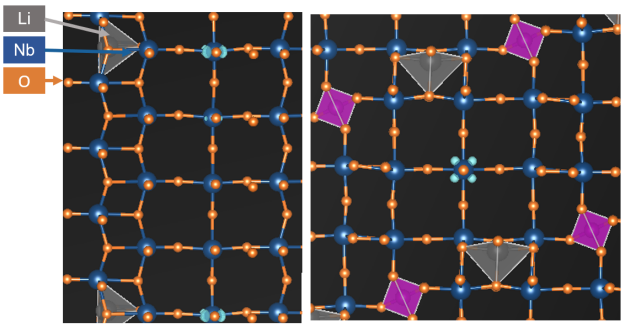

Figure 10: Charge density of the electron denoted by Li in $Li_{0.25}PNb_9O_{25}$ having a $1\times1\times4$ super cell of the PNb_9O_{25} primitive cell. The donated electrons localize on a Nb of a corner sharing octahedron at the center of the $3\times3\times\infty$ perovskite block. (Left panel is a side view of the crystal, with the c axis pointing up while the right panel is a view down the c axis.)

bond formation, which is made possible by the overlap of t_{2g}-like orbitals between the metals of edge-sharing octahedra. The charge density plots also suggest an increase in the degree of electron delocalization, which is expected to enhance electronic conductivity.[9]

A similar progression of orbital filling was predicted by Kocer et al.[22] in their study of Wadsley-Roth phases containing Nb and W. They pointed out that the electrons donated by Li first accumulate on localized, non-bonding t_{2g} orbitals at the center of the blocks before they start filling t_{2g} levels on the edge-sharing transition metals. This order of orbital filling has also been used to explain the origin of the insulator-metal transition at low Li concentrations in $Li_xPNb_9O_{25}$.[9]

Filling of the t_{2g} orbitals of the edge-sharing NbO_6 octahedra plays an important role in effecting the structural changes that occur as the Li concentration of the host increases, including the shortening of the Nb-Nb bond lengths between edge-sharing NbO_6 octahedra and an increase in the e_3 strain order parameter. The Nb of the edge-sharing blocks are distorted away from the centers of the octahedra in PNb_9O_{25}. The off-centering is likely a result of a combination of factors.[22] The Nb^{5+} oxidation state makes the cation susceptible to a second-order Jahn-Teller distortion, which leads to cation off-centering in octahedral environments. The off-centering may also arise from an electrostatic repulsion between edge-sharing Nb^{5+} cations, biasing the off-centering in directions that increase the Nb-Nb distance. As electrons fill the edge sharing t_{2g} levels, the effective valence of the Nb is no longer 5+ but progressively becomes closer to 4+ and then 3+.

This should lead to a reduction in electrostatic repulsion between edge-sharing Nb and eliminate the susceptibility for second order Jahn-Teller distortions. Furthermore, the t_{2g} orbitals of the edge-sharing NbO_6 octahedra appear to form metal-metal bonds beyond x=7 (Figure 11), which should also tend to shorten Nb-Nb distances. The shortening of the Nb-Nb distances along the block peripheries relieve the distortions of the NbO_6 octahedra. As a consequence, the W_v vertical window sites become less distorted making them more amenable for Li occupancy. It is likely that these structural changes in response to electron filling are responsible for the stability of the interweaved ordering that forms a backbone of the majority of low energy structures between x=7 and x=14. Density of states and charge densities for low energy structures between x=4 and 7 are shown in the Supplementary Information (Figure S20)

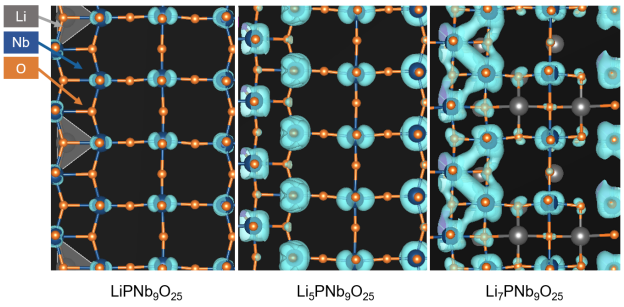

Figure 11: Charge density along the edge-sharing niobium octahedral sites with increasing composition. The charge density is viewed perpendicular to the c lattice vector. At low compositions, electrons localize on the central, corner-sharing niobium in the middle of the perovskite blocks. As more electrons are added at higher Li concentrations, electrons begin filling d orbitals in the edge-sharing NbO_6 octahedra and delocalize. Increasing electron delocalization occurs in conjunction with decreasing edge-sharing niobium-niobium distances and increasing values of the e_3 strain order parameter.

Discussion

The Wadsley-Roth phases are a promising class of anode materials for high power Li-ion batteries. They exhibit a rich variety of open crystal structures that can host Li ions over multiple types of interstitial sites. A common structural feature among all Wadsley-Roth phases are their blocks of corner sharing octahedra that are held together by edge-sharing octahedra. While they have

impressive electrochemical properties and can accommodate more than one Li per transition metal, very little is known about the mechanisms of Li insertion into Wadsley-Roth phases.

The results of our study on $Li_xPNb_9O_{25}$ show that the electronic and thermodynamic properties associated with Li insertion into Wadsley-Roth phases is more complex than those of most other common intercalation compounds.[71,72] PNb_9O_{25} can host Li in five symmetrically distinct sites, three of which have pyramidal coordination by oxygen (P_s, P_e and P_c) and two that are coordinated by four coplanar oxygen ions (W_v and W_h) also known as window sites.[22,60] An important prediction of this work is the occurrence of a site preference inversion upon Li insertion into PNb_9O_{25}. Using an iterative approach that relies on the cluster expansion method to extrapolate computationally expensive DFT calculations, we predict that Li initially fills the P_s and P_e pyramidal sites, but that these sites fall out of favor at higher Li concentrations where Li first fills the P_c sites (with some residual occupancy on the P_e sites) and then gradually fills the two window sites, W_v and W_h. Only at much higher Li concentrations ($x \approx 8$) does Li return to the P_s sites. The site inversion from P_s and P_e at x=2 to predominantly P_c at x=4 is responsible for a plateau in the voltage curve at low Li concentrations. The plateau is present in both the experimental voltage curve[8,9] as well as the calculated voltage curve and appears to be a common feature of many other similar Wadsley-Roth phases. Our neutron diffraction refinements, while somewhat ambiguous in its assignments of site occupancy over the pyramidal sites, P_s, P_e and P_c, do not contradict our DFT predictions. Furthermore, the neutron diffraction refinements unequivocally confirm that Li does not fill window sites during the early stages of Li insertion (i.e. $x < 4.3$).

A second important prediction of this study is the stability of the interweaved backbone ordering over the W_v vertical window sites that sets in between $7 < x < 14$ and is present in almost all ground states and low energy Li-vacancy orderings in that concentration interval. The interweaved ordering leads to a doubling of the unit cell along the c-axis. While the ordering on average remains locked in place over a wide concentration interval, the remaining W_h and P_s sites accommodate Li in a disordered manner. This leads to a unique intercalation process in which Li orders over one sublattice (i.e. W_v) but forms a solid solution over other sublattices

(W_h and P_s). The result is a sloping voltage profile that is characteristic of a solid solution, with occasional kinks due to secondary ordering tendencies over the W_h and P_s sites. The influence of this partial ordering on kinetic properties is likely to be significant and will be the focus of future studies. Our DFT calculations predict that the interweaved backbone ordering can easily tolerate defects whereby pairs of Li in W_v sites in a given layer rearrange and occupy W_v sites that form a 90^o angle with each other (as opposed to pairs of W_v sites that form a 180^o angle with each other in the interweaved ordering). The preference for window sites at higher Li concentrations is consistent with neutron diffraction studies of other Wadsley-Roth phases by Catti et al.[60–62]

Our calculations have also shown that changes in electronic structure due to the filling of the t_{2g} levels upon Li insertion results in structural distortions that in turn affect Li-site preferences. The Nb of the edge-sharing octahedra distort off-center in the pristine PNb_9O_{25} compound, likely due to a combination of factors that includes a second-order Jahn-Teller distortion of the Nb^{5+} cations within their octahedra and electrostatic interactions between edge-sharing Nb^{5+} cations.[22] This leads to highly distorted NbO_6 octahedra that then distort the neighboring W_v vertical window sites, making them unfavorable for Li occupancy. The addition of electrons to the host upon Li insertion reduces the Nb^{5+} to lower oxidation states, thereby eliminating the susceptibility for second-order Jahn-Teller distortions and promoting the formation of metal-metal bonds between edge-sharing Nb. The combination of these factors results in a shortening of Nb-Nb distances between edge-sharing octahedra and a reduction in the degree with which the octahedra are distorted. As a result, the W_v sites become more square planar and therefore more favorable. Our calculations clearly show that it is only after the structural distortions of the edge-sharing octahedra are eliminated beyond x=7 that the filling of the W_v vertical window sites sets in. Similar behavior has been observed in other Wadsley-Roth phases by Griffith et al.[6,12] and Kocer et. al.[22,63,70], who found an increased stability of the window sites due to the disappearance of the distortions of the edge-sharing transition metal-oxygen octahedra at high Li concentrations. The phenomenon has also been noted in other intercalation compounds such as anatase TiO_2, where the elimination of structural distortions due to the reduction of Ti was shown

to deleteriously affect Li diffusion kinetics.[73] Our results taken together with the earlier work of Kocer et al.[22,63,70] suggests that the coupling between electronic structure and crystallographic distortions is a common phenomenon of Wadsley-Roth phases.

The ability to predict stable Li-site preferences and ordering tendencies in Wadsley-Roth phases is made especially challenging by the combinatorial explosion of all the possible ways of distributing Li ions and vacancies over the many sites of these phases. The number of Li-vacancy orderings within the primitive cell of PNb_9O_{25}, for example, is already 2^{20} or 1,048,576 due to the fact that the primitive cell contains 20 candidate Li sites. Often stable orderings form in super cells of the primitive cell. The doubling of the PNb_9O_{25} unit cell along the c-axis, for instance, increases the number of candidate Li-vacancy orderings to 2^{40} or over 10^{12}. Overcoming these combinatorial challenges requires tools such as the cluster expansion, as they allow for a rapid search over configuration space with Monte Carlo techniques to identify low energy Li-vacancy orderings. It should be noted, however, that while cluster expansions are generally superior to other approaches that screen candidate orderings based on electrostatic energy, for example, they are not necessarily exhaustive. The approach is iterative, whereby cluster expansions are trained to an ever increasing database of first-principles energies to increase their predictive accuracy. As with any method that relies on extrapolation, however, there is no guarantee that it accurately predicts the true ground state Li-vacancy orderings.

While the calculated and measured voltage curves of Figure 6 show reasonable qualitative agreement, there is a systematic under prediction above x=2. This is not unexpected as DFT-PBE is known to systematically under predict voltages.[43,74] Below x=2, the quantitative agreement is better, however, the shape of the calculated voltage profile differs from the experimental one (Figure 6). The experimental voltage curve exhibits a small plateau followed by a step around x=0.5 that is not present in the calculated voltage curve. The discrepancy may arise from the neglect of additional degrees of freedom in the statistical mechanics calculation of the room temperature voltage curve. $Li_xPNb_9O_{25}$ undergoes an insulator to metal transition at low Li concentrations that may require more accurate electronic structure methods to describe correctly. Our DFT-PBE

calculations already indicate a high degree of electron localization at very dilute concentrations. It is possible that these localized states may have a high degree of degeneracy with respect to their placement within the crystal, leading to an additional source of configurational entropy that was not accounted for in this study. A similar phenomenon was proposed to explain the role of the metal-insulator transition in causing a two-phase reaction in Li_xCoO_2 between x=0.93 and x=0.75.[75] It is suggested that the electronic properties of $Li_xPNb_9O_{25}$ at dilute Li concentrations receive further attention both experimentally and theoretically.

Conclusion

We have performed a first-principles statistical mechanics study of the electrochemical properties of PNb_9O_{25} as a function of Li concentration. PNb_9O_{25}, which is a Wadsley-Roth phase made of $3\times3\times\infty$ perovskite-like blocks, can host Li in three symmetrically distinct types of pyramidal sites at the block edges and two types of window sites within the blocks. Our first-principles DFT-PBE calculations predict that Li initially prefers pyramidal sites, only filling the window sites at intermediate to high Li concentrations. Neutron diffraction is consistent with DFT predictions of pyramidal site occupancy at low Li concentrations. The window sites only become favorable after the host undergoes a tetragonal distortion due to a chemical strain that accompanies Li insertion. The tetragonal distortion of the host is found to correlate with the filling of Nb d orbitals in the edge-sharing NbO_6 octahedra, which relieves second-order Jahn-Teller distortions and leads to metal-metal bonding. The lowest energy configurations above x=7 are found to share a common Li-vacancy ordering motif over the vertical window sites, with the other sites accommodating Li as a solid solution. Our predictions of the sequence of site filling and the nature of Li-vacancy ordering in PNb_9O_{25} set the stage for studies of Li diffusion mechanisms within this complex host. Due to the vast structural similarities among different Wadsley-Roth phases, many of our findings for PNb_9O_{25} should also apply to other Wadsley-Roth phase chemistries.

Supplementary Information

Time-of-flight data, Neutron Diffraction Rietveld fits and fit comparisons, and neutron pair distribution function data can all be found in the Supplementary Information. The zero kelvin voltage curve as calculated with SCAN meta GGA density functional theory, schematics of the ground state orderings as predicted with DFT-PBE, comparisons of the DFT-PBE and cluster expansion formation energies, strain order parameters as a function of Li concentration, molecular orbital diagrams and charge density plots of ground state orderings between x=4 and x=7 are also in the Supplementary Information.

Acknowledgements

This work was supported as part of the Center for Synthetic Control Across Length-scales for Advancing Rechargeables (SCALAR), an Energy Frontier Research Center funded by the U.S. Department of Energy, Office of Science, Basic Energy Sciences under Award DE-SC0019381. This work made use of the UC Santa Barbara Materials Research Laboratory's Shared Experimental Facilities, which are supported by the MRSEC Program of the NSF under Award No. DMR 1720256; a member of the NSF-funded Materials Research Facilities Network (www.mrfn.org). This research used resources at the Spallation Neutron Source, a DOE Office of Science User Facility operated by the Oak Ridge National Laboratory. We acknowledge the Center for Scientific Computing (CSC) from the CNSI, MRL, and NSF MRSEC (grant DMR-1121053) for providing computing resources. We are grateful for supercomputing resources at the National Energy Research Scientific Computing Center (NERSC), a DOE Office of Science user facility supported by the U.S. Department of Energy Office of Science (grant DE-AC02-05CH11231). We thank the instrument scientists at NOMAD (BL-1B, Spallation Neutron Source, Oak Ridge National Laboratory), Michelle Everett and Joerg Neuefeind, for collecting the data and for data pre-processing. We thank Partha Paul for useful discussions regarding diffraction. We thank Julija Vinckevičiūtė, Jonas L. Kaufman, Naga Sri Harsha Gunda, and Farnaz Kaboudvand for valuable insights. Additionally, we thank

Jon Gabriel Goiri for coding assistance as well as Colleen Reynolds for helpful discussion on the Wadsley-Roth phases.

References

(1) Zubi, G.; Dufo-López, R.; Carvalho, M.; Pasaoglu, G. The lithium-ion battery: State of the art and future perspectives. *Renewable Sustainable Energy Rev.* **2018**, *89*, 292 – 308.

(2) Vetter, J.; Novák, P.; Wagner, M. R.; Veit, C.; Möller, K.-C.; Besenhard, J.; Winter, M.; Wohlfahrt-Mehrens, M.; Vogler, C.; Hammouche, A. Ageing mechanisms in lithium-ion batteries. *J. Power Sources* **2005**, *147*, 269–281.

(3) Downie, L. E.; Krause, L. J.; Burns, J. C.; Jensen, L. D.; Chevrier, V. L.; Dahn, J. R. In situ detection of lithium plating on graphite electrodes by electrochemical calorimetry. *J. Electrochem. Soc.* **2013**, *160*, A588.

(4) Rajendran, S.; Pilli, A.; Omolere, O.; Kelber, J.; Arava, L. M. R. An All-Solid-State Battery with a Tailored Electrode–Electrolyte Interface Using Surface Chemistry and Interlayer-Based Approaches. *Chem. Mater.* **2021**, *33(9)*, 3401–3412.

(5) Fantin, R.; Trevisanello, E.; Ruess, R.; Pokle, A.; Conforto, G.; Richter, F. H.; Volz, K.; Janek, J. Synthesis and Postprocessing of Single-Crystalline $LiNi_{0.8}Co_{0.15}Al_{0.05}O_2$ for Solid-State Lithium-Ion Batteries with High Capacity and Long Cycling Stability. *Chem. Mater.* **2021**, *33(7)*, 2624–2634.

(6) Griffith, K. J.; Wiaderek, K. M.; Cibin, G.; Marbella, L. E.; Grey, C. P. Niobium tungsten oxides for high-rate lithium-ion energy storage. *Nature* **2018**, *559*, 556–563.

(7) Cava, R. J.; Murphy, D. W.; Zahurak, S. M. Lithium insertion in Wadsley-Roth phases based on niobium oxide. *J. Electrochem. Soc.* **1983**, *130*, 2345.

(8) Patoux, S.; Dolle, M.; Rousse, G.; Masquelier, C. A Reversible Lithium Intercalation Process in an ReO_3 Type Structure PNb_9O_{25}. *J. Electrochem. Soc.* **2002**, *149*, A391.

(9) Preefer, M. B.; Saber, M.; Wei, Q.; Bashian, N. H.; Bocarsly, J. D.; Zhang, W.; Lee, G.; Milam-Guerrero, J.; Howard, E. S.; Vincent, R. C., et al. Multielectron Redox and Insulator-to-Metal Transition upon Lithium Insertion in the Fast-Charging,

Wadsley-Roth Phase PNb_9O_{25}. *Chem. Mater.* **2020**, *32(11)*, 4553–4563.

(10) Lu, X.; Jian, Z.; Fang, Z.; Gu, L.; Hu, Y.-S.; Chen, W.; Wang, Z.; Chen, L. Atomic-scale investigation on lithium storage mechanism in $TiNb_2O_7$. *Energy Environ. Sci.* **2011**, *4*, 2638–2644.

(11) Guo, B.; Yu, X.; Sun, X.-G.; Chi, M.; Qiao, Z.-A.; Liu, J.; Hu, Y.-S.; Yang, X.-Q.; Goodenough, J. B.; Dai, S. A long-life lithium-ion battery with a highly porous $TiNb_2O_7$ anode for large-scale electrical energy storage. *Energy Environ. Sci.* **2014**, *7*, 2220–2226.

(12) Griffith, K. J.; Seymour, I. D.; Hope, M. A.; Butala, M. M.; Lamontagne, L. K.; Preefer, M. B.; Kocer, C. P.; Henkelman, G.; Morris, A. J.; Cliffe, M. J., et al. Ionic and electronic conduction in $TiNb_2O_7$. *J. Am. Chem. Soc.* **2019**, *141*, 16706–16725.

(13) Han, J.-T.; Goodenough, J. B. 3-V full cell performance of anode framework $TiNb_2O_7$/spinel $LiNi_{0.5}Mn_{1.5}O_4$. *Chem. Mater.* **2011**, *23*, 3404–3407.

(14) Cheng, Q.; Liang, J.; Zhu, Y.; Si, L.; Guo, C.; Qian, Y. Bulk $Ti_2Nb_{10}O_{29}$ as long-life and high-power Li-ion battery anodes. *J. Mater. Chem. A* **2014**, *2*, 17258–17262.

(15) Wu, X.; Miao, J.; Han, W.; Hu, Y.-S.; Chen, D.; Lee, J.-S.; Kim, J.; Chen, L. Investigation on $Ti_2Nb_{10}O_{29}$ anode material for lithium-ion batteries. *Electrochem. Commun.* **2012**, *25*, 39–42.

(16) Li, Y.; Sun, C.; Goodenough, J. B. Electrochemical lithium intercalation in monoclinic $Nb_{12}O_{29}$. *Chem. Mater.* **2011**, *23*, 2292–2294.

(17) Li, R.; Qin, Y.; Liu, X.; Yang, L.; Lin, C.; Xia, R.; Lin, S.; Chen, Y.; Li, J. Conductive $Nb_{25}O_{62}$ and $Nb_{12}O_{29}$ anode materials for use in high-performance lithium-ion storage. *Electrochim. Acta* **2018**, *266*, 202–211.

(18) Saritha, D.; Pralong, V.; Varadaraju, U. V.; Raveau, B. Electrochemical Li insertion studies on $WNb_{12}O_{33}$—A shear ReO_3 type structure. *J. Solid State Chem.* **2010**, *183*, 988–993.

(19) Yan, L.; Lan, H.; Yu, H.; Qian, S.; Cheng, X.; Long, N.; Zhang, R.; Shui, M.; Shu, J.

Electrospun $WN_{12}O_{33}$ nanowires: superior lithium storage capability and their working mechanism. *J. Mater. Chem. A* **2017**, *5*, 8972–8980.

(20) Fuentes, A. F.; Garza, E. B.; de la Cruz, A. M.; Torres-Martínez, L. M. Lithium and sodium insertion in $W_3Nb_{14}O_{44}$, a block structure type phase. *Solid State Ionics* **1997**, *93*, 245–253.

(21) Yan, L.; Shu, J.; Li, C.; Cheng, X.; Zhu, H.; Yu, H.; Zhang, C.; Zheng, Y.; Xie, Y.; Guo, Z. $W_3Nb_{14}O_{44}$ nanowires: Ultrastable lithium storage anode materials for advanced rechargeable batteries. *Energy Storage Materials* **2019**, *16*, 535–544.

(22) Koçer, C. P.; Griffith, K. J.; Grey, C. P.; Morris, A. J. Cation Disorder and Lithium Insertion Mechanism of Wadsley–Roth Crystallographic Shear Phases from First Principles. *J. Am. Chem. Soc.* **2019**, *141*, 15121–15134.

(23) Cao, D.; Yao, Z.; Liu, J.; Zhang, J.; Li, C. H-Nb_2O_5 wired by tetragonal tungsten bronze related domains as high-rate anode for Li-ion batteries. *Energy Storage Materials* **2018**, *11*, 152–160.

(24) Viet, A. L.; Reddy, M. V.; Jose, R.; Chowdari, B. V. R.; Ramakrishna, S. Nanostructured Nb_2O_5 polymorphs by electrospinning for rechargeable lithium batteries. *J. Phys. Chem. C* **2010**, *114*, 664–671.

(25) Kodama, R.; Terada, Y.; Nakai, I.; Komaba, S.; Kumagai, N. Electrochemical and in situ XAFS-XRD investigation of Nb_2O_5 for rechargeable lithium batteries. *J. Electrochem. Soc.* **2006**, *153*, A583.

(26) Augustyn, V.; Come, J.; Lowe, M. A.; Kim, J. W.; Taberna, P.-L.; Tolbert, S. H.; Abruña, H. D.; Simon, P.; Dunn, B. High-rate electrochemical energy storage through Li+ intercalation pseudocapacitance. *Nat. Mater.* **2013**, *12*, 518–522.

(27) Kim, J. W.; Augustyn, V.; Dunn, B. The effect of crystallinity on the rapid pseudocapacitive response of Nb_2O_5. *Adv. Energy Mater.* **2012**, *2*, 141–148.

(28) Jiang, J.; Dahn, J. R. Dependence of the heat of reaction of $Li_{0.81}C_6$ (0.1 V), $Li_7Ti_5O_{12}$ (1.55 V), and $Li_{0.5}VO_2$ (2.45 V) reacting with nonaqueous solvents or electrolytes on the average potential of

the electrode material. *J. Electrochem. Soc.* **2005**, *153*, A310.

(29) Kresse, G.; Hafner, J. Ab initio molecular dynamics for liquid metals. *Phys. Rev. B* **1993**, *47*, 558.

(30) Kresse, G.; Hafner, J. Ab initio molecular-dynamics simulation of the liquid-metal–amorphous-semiconductor transition in germanium. *Phys. Rev. B* **1994**, *49*, 14251.

(31) Kresse, G.; Furthmüller, J. Efficient iterative schemes for ab initio total-energy calculations using a plane-wave basis set. *Phys. Rev. B* **1996**, *54*, 11169.

(32) Kresse, G.; Furthmüller, J. Efficiency of ab-initio total energy calculations for metals and semiconductors using a plane-wave basis set. *Comput. Mater. Sci.* **1996**, *6*, 15–50.

(33) Perdew, J. P.; Burke, K.; Ernzerhof, M. Generalized gradient approximation made simple. *Phys. Rev. Lett.* **1996**, *77*, 3865.

(34) Strongly constrained and appropriately normed semilocal density functional, author=Sun, Jianwei and Ruzsinszky, Adrienn and Perdew, John P. *Phys. Rev. Lett.* **2015**, *115*, 036402.

(35) Sun, J.; Remsing, R. C.; Zhang, Y.; Sun, Z.; Ruzsinszky, A.; Peng, H.; Yang, Z.; Paul, A.; Waghmare, U.; Wu, X., et al. Accurate first-principles structures and energies of diversely bonded systems from an efficient density functional. *Nat. Chem.* **2016**, *8*, 831.

(36) Blöchl, P. E. Projector augmented-wave method. *Phys. Rev. B* **1994**, *50*, 17953.

(37) Kresse, G.; Joubert, D. From ultrasoft pseudopotentials to the projector augmented-wave method. *Phys. Rev. B* **1999**, *59*, 1758.

(38) Momma, K.; Izumi, F. VESTA 3 for three-dimensional visualization of crystal, volumetric and morphology data. *J. Appl. Crystallogr.* **2011**, *44*, 1272–1276.

(39) Puchala, B.; Van der Ven, A. Thermodynamics of the Zr-O system from first-principles calculations. *Phys. Rev. B* **2013**, *88*, 094108.

(40) Thomas, J. C.; Van der Ven, A. Finite-temperature properties of strongly anharmonic and mechanically unstable crystal

phases from first principles. *Phys. Rev. B* **2013**, *88*, 214111.

(41) Van der Ven, A.; Thomas, J. C.; Puchala, B.; Natarajan, A. R. First-principles statistical mechanics of multicomponent crystals. *Annu. Rev. Mater. Res.* **2018**, *48*, 27–55.

(42) CASM Developers, CASM, v0.2.1. Available from https:// github.com/prisms-center/CASMcode, 2018.

(43) Van der Ven, A.; Deng, Z.; Banerjee, S.; Ong, S. P. Rechargeable alkali-ion battery materials: theory and computation. *Chem. Rev. (Washington, DC, U. S.)* **2020**, *120*, 6977–7019.

(44) Van der Ven, A.; Thomas, J. C.; Xu, Q.; Swoboda, B.; Morgan, D. Nondilute diffusion from first principles: Li diffusion in Li_xTiS_2. *Phys. Rev. B* **2008**, *78*, 104306.

(45) Bhattacharya, J.; Van der Ven, A. First-principles study of competing mechanisms of nondilute Li diffusion in spinel Li_xTiS_2. *Phys. Rev. B* **2011**, *83*, 144302.

(46) Chang, D.; Huo, H.; Johnston, K. E.; Ménétrier, M.; Monconduit, L.; Grey, C. P.; Van der Ven, A. Elucidating the origins of phase transformation hysteresis during electrochemical cycling of Li–Sb electrodes. *J. Mater. Chem. A* **2015**, *3*, 18928–18943.

(47) Chang, D.; Chen, M.-H.; Van der Ven, A. Factors contributing to path hysteresis of displacement and conversion reactions in Li ion batteries. *Chem. Mater.* **2015**, *27*, 7593–7600.

(48) Emly, A.; Van der Ven, A. Mg intercalation in layered and spinel host crystal structures for Mg batteries. *Inorg. Chem.* **2015**, *54*, 4394–4402.

(49) Vinckeviciute, J.; Radin, M. D.; Van der Ven, A. Stacking-sequence changes and Na ordering in layered intercalation materials. *Chem. Mater.* **2016**, *28*, 8640–8650.

(50) Kolli, S. K.; Van der Ven, A. Controlling the electrochemical properties of spinel intercalation compounds. *ACS Appl. Energy Mater.* **2018**, *1*, 6833–6839.

(51) Kolli, S. K.; Van der Ven, A. First-principles study of spinel $MgTiS_2$ as a cathode material. *Chem. Mater.* **2018**, *30*, 2436–2442.

(52) Kaufman, J. L.; Van der Ven, A. Na_xCoO_2

phase stability and hierarchical orderings in the O3/P3 structure family. *Phys. Rev. Mater.* **2019**, *3*, 015402.

(53) Kaufman, J. L.; Van der Ven, A. Ordering and Structural Transformations in Layered K_xCrO_2 for K-Ion Batteries. *Chem. Mater.* **2020**, *32*, 6392–6400.

(54) Toby, B. H.; Von Dreele, R. B. GSAS-II: the genesis of a modern open-source all purpose crystallography software package. *J. Appl. Crystallogr.* **2013**, *46*, 544–549.

(55) Benabbas, A.; Borel, M. M.; Grandin, A.; Leclaire, A.; Raveau, B. Redetermination of the structure of PNb_9O_{25}. *Acta Crystallogr., Sect. C: Cryst. Struct. Commun.* **1991**, *47*, 849–850.

(56) Farrow, C. L.; Juhas, P.; Liu, J. W.; Bryndin, D.; Božin, E. S.; Bloch, J.; Proffen, T.; Billinge, S. J. L. PDFfit2 and PDFgui: computer programs for studying nanostructure in crystals. *J. Phys.: Condens. Matter* **2007**, *19*, 335219.

(57) Roth, R. S.; Wadsley, A. D.; Andersson, S. The crystal structure of PNb_9O_{25} (P_2O_5. $9Nb_2O_5$). *Acta Crystallogr.* **1965**, *18*, 643–647.

(58) Cava, R. J.; Santoro, A.; Murphy, D.; Zahurak, S.; Roth, R. The structures of the lithium inserted metal oxides $Li_{0.2}ReO_3$ and $Li_{0.36}WO_3$. *J. Solid State Chem.* **1983**, *50*, 121–128.

(59) Bashian, N. H.; Zhou, S.; Zuba, M.; Ganose, A. M.; Stiles, J. W.; Ee, A.; Ashby, D. S.; Scanlon, D. O.; Piper, L. F.; Dunn, B., et al. Correlated polyhedral rotations in the absence of polarons during electrochemical insertion of lithium in ReO_3. *ACS Energy Lett.* **2018**, *3*, 2513–2519.

(60) Catti, M.; Ghaani, M. R. On the lithiation reaction of niobium oxide: structural and electronic properties of Li 1.714 Nb 2 O 5. *Physical Chemistry Chemical Physics* **2014**, *16*, 1385–1392.

(61) Pinus, I.; Catti, M.; Ruffo, R.; Salamone, M. M.; Mari, C. M. Neutron diffraction and electrochemical study of $FeNb_{11}O_{29}$/$Li_{11}FeNb_{11}O_{29}$ for lithium battery anode applications. *Chem. Mater.* **2014**, *26*, 2203–2209.

(62) Catti, M.; Pinus, I.; Knight, K. Lithium insertion properties of $Li_xTiNb_2O_7$ investigated by neutron diffraction and first-principles modelling. *J. Solid State Chem.* **2015**, *229*, 19–25.

(63) Koçer, C. P.; Griffith, K. J.; Grey, C. P.; Morris, A. J. First-principles study of localized and delocalized electronic states in crystallographic shear phases of niobium oxide. *Phys. Rev. B* **2019**, *99*, 075151.

(64) Van der Ven, A.; Thomas, J. C.; Xu, Q.; Bhattacharya, J. Linking the electronic structure of solids to their thermodynamic and kinetic properties. *Mathematics and computers in simulation* **2010**, *80*, 1393–1410.

(65) Yu, H.; Zhang, J.; Zheng, R.; Liu, T.; Peng, N.; Yuan, Y.; Liu, Y.; Shu, J.; Wang, Z.-B. The journey of lithium ions in the lattice of PNb_9O_{25}. *Mater. Chem. Front.* **2020**, *4*, 631–637.

(66) Kondrakov, A. O.; Schmidt, A.; Xu, J.; Geßwein, H.; Monig, R.; Hartmann, P.; Sommer, H.; Brezesinski, T.; Janek, J. Anisotropic lattice strain and mechanical degradation of high-and low-nickel NCM cathode materials for Li-ion batteries. *J. Phys. Chem. C* **2017**, *121*, 3286–3294.

(67) Thackeray, M. M.; Shao-Horn, Y.; Kahaian, A. J.; Kepler, K. D.; Skinner, E.; Vaughey, J. T.; Hackney, S. A. Structural Fatigue in Spinel Electrodes in High Voltage (4 V) $Li/Li_xMn_2O_4$ Cells. *Electrochem. Solid-State Lett.* **1998**, *1*, 7.

(68) Thomas, J. C.; Van der Ven, A. The exploration of nonlinear elasticity and its efficient parameterization for crystalline materials. *J. Mech. Phys. Solids* **2017**, *107*, 76–95.

(69) Goiri, J. G.; Van der Ven, A. Phase and structural stability in Ni-Al systems from first principles. *Phys. Rev. B* **2016**, *94*, 094111.

(70) Koçer, C. P.; Griffith, K. J.; Grey, C. P.; Morris, A. J. Lithium diffusion in niobium tungsten oxide shear structures. *Chem. Mater.* **2020**, *32*, 3980–3989.

(71) Radin, M. D.; Van der Ven, A. Stability of prismatic and octahedral coordination in layered oxides and sulfides interca-

lated with alkali and alkaline-earth metals. *Chem. Mater.* **2016**, *28*, 7898–7904.

(72) Radin, M. D.; Hy, S.; Sina, M.; Fang, C.; Liu, H.; Vinckeviciute, J.; Zhang, M.; Whittingham, M. S.; Meng, Y. S.; Van der Ven, A. Narrowing the gap between theoretical and practical capacities in Li-ion layered oxide cathode materials. *Adv. Energy Mater.* **2017**, *7*, 1602888.

(73) Belak, A. A.; Wang, Y.; Van der Ven, A. Kinetics of anatase electrodes: the role of ordering, anisotropy, and shape memory effects. *Chem. Mater.* **2012**, *24*, 2894–2898.

(74) Isaacs, E. B.; Patel, S.; Wolverton, C. Prediction of Li intercalation voltages in rechargeable battery cathode materials: Effects of exchange-correlation functional, van der Waals interactions, and Hubbard U. *Phys. Rev. Mater.* **2020**, *4*, 065405.

(75) Van der Ven, A.; Aydinol, M. K.; Ceder, G.; Kresse, G.; Hafner, J. First-principles investigation of phase stability in Li_xCoO_2. *Phys. Rev. B* **1998**, *58*, 2975.

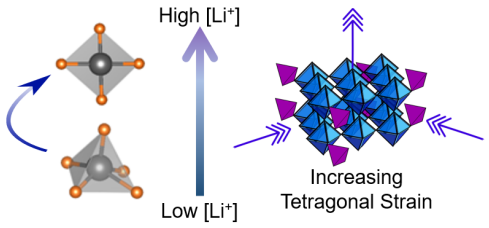
High [Li+]
Low [Li+]
Increasing
Tetragonal Strain

SI for The role of electronic structure on Li-ordering and chemical strain in the fast charging Wadsley-Roth phase PNb_9O_{25}

Muna Saber,[†] Molleigh B. Preefer,[‡] Sanjeev K. Kolli,[¶] William Zhang,[§] Geneva Laurita,[‖] Bruce Dunn,[⊥] Ram Seshadri,[¶,§] and Anton Van der Ven[*,¶]

†*Department of Chemical Engineering, University of California, Santa Barbara, Santa Barbara, California 93106, USA*

‡*SLAC National Accelerator Laboratory, Menlo Park, California 95025, USA*

¶*Materials Department, University of California, Santa Barbara, Santa Barbara, California 93106, USA*

§*Department of Chemistry and Biochemistry, University of California, Santa Barbara, Santa Barbara, California 93106, USA*

‖*Department of Chemistry and Biochemistry, Bates College, Lewiston, Maine 04240, USA*

⊥*Department of Materials Science and Engineering, University of California Los Angeles, Los Angeles, California 90095, USA*

E-mail: avdv@ucsb.edu

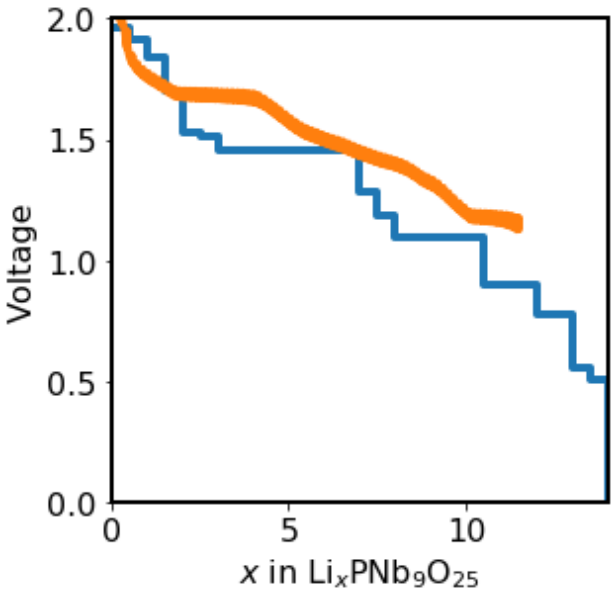

Figure 1: Voltage curve at 0 Kelvin (blue lines) as calculated with SCAN along with the experimental voltage curve at room temperature (orange curve). Energies were calculated for the ground states as determined with DFT-PBE. Vertical lines correspond to stable ground states and horizontal lines correspond to two-phase regions. SCAN predicted voltages are overall higher than those predicted with PBE.

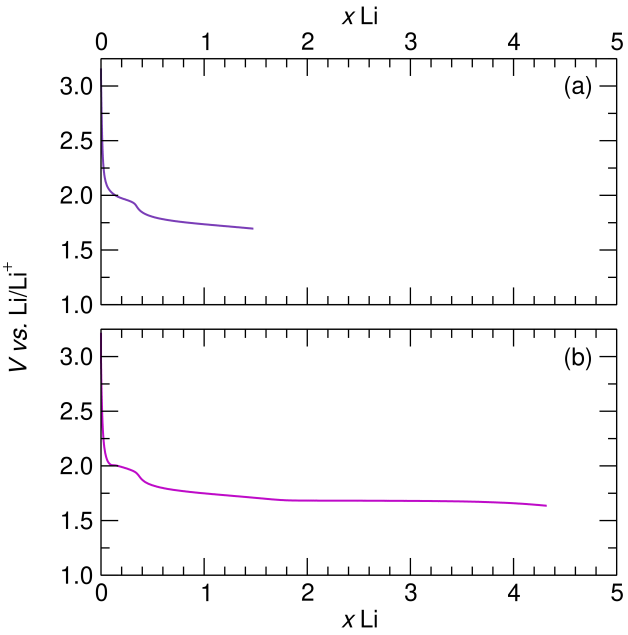

Figure 2: Galvanostatic discharge of PNb_9O_{25} in large format, loose powder Swagelok cells. Each cell contained an average of 200 mg of the electrode mixture (160 mg of active material). The cells were discharged at a rate of C/80 with a lower voltage cutoff of (a) 1.695 V and (b) 1.635 in order to capture the structural changes before and after the main plateau at 1.65 V. The electrochemistry seen here directly corresponds to the samples used for all of the refinements.

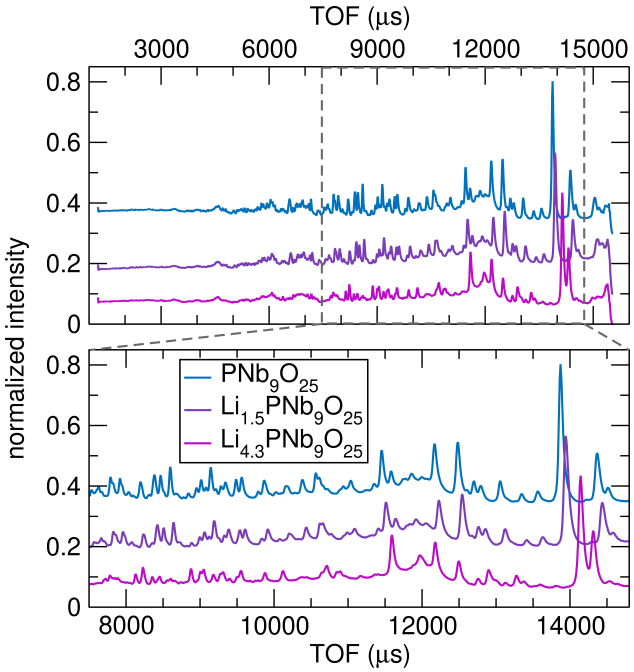

Figure 3: Time-of-flight data for PNb_9O_{25}, $Li_{1.5}PNb_9O_{25}$, and $Li_{4.3}Nb_9O_{25}$ collected at the Spallation Neutron Source at Oak Ridge National Lab (NOMAD, wavelength = 1.4 Angstroms) (a) in the full range of data collection for bank 5, and (b) the selected range used for refinements. The range was chosen to capture a consistent range of complete, well-defined peaks between all samples.

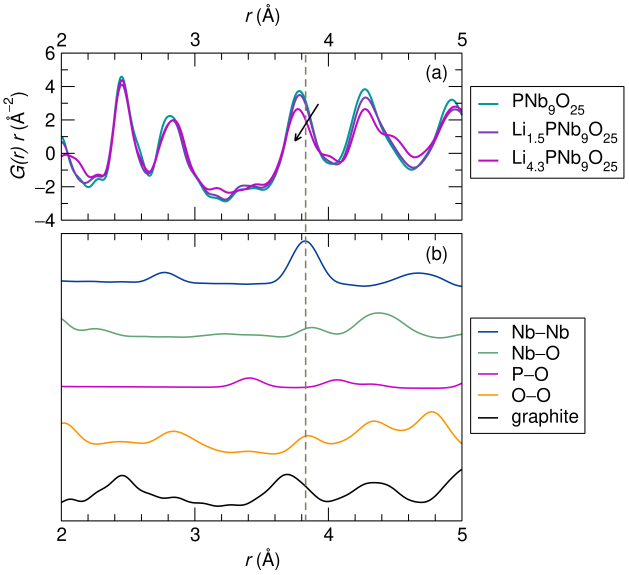

Figure 4: (a) Neutron pair distribution function data of PNb_9O_{25}, $Li_{1.5}PNb_9O_{25}$, and $Li_{4.3}PNb_9O_{25}$ from 2-5 Å. The arrow points to the shifting of the peak at 3.8 Å to shorter distances. (b) Calculated atomic distances for all of the atom pairs from the known crystallographic structure of PNb_9O_{25} (space group I 4/m, 87) showing the deconvolution of each peak. The peak centered at 3.81 Å corresponds to the Nb-Nb atomic distance, marked with a grey dashed line. The shift in the peak at 3.8 Å in $Li_{4.3}PNb_9O_{25}$ to shorter distances supports the result from DFT that Nb-Nb distances become shorter with lithiation.

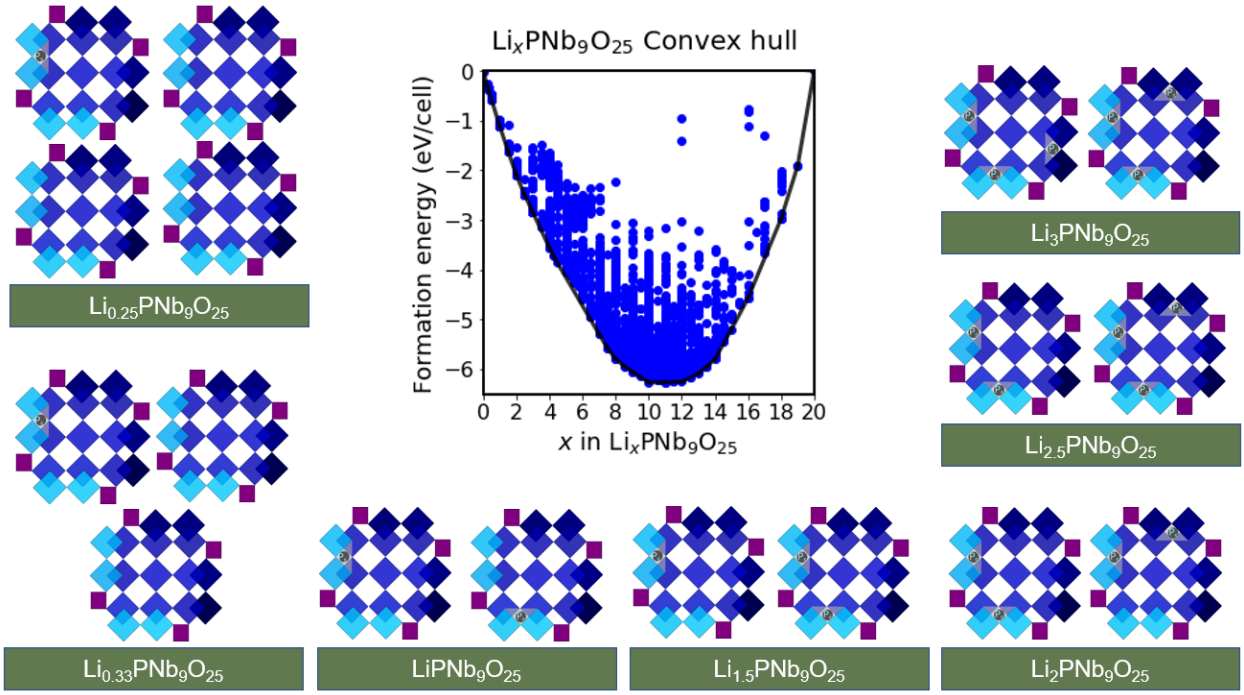

Figure 5: Formation energies and schematics of ground state orderings of $Li_xPNb_9O_{25}$ at low compositions as determined with DFT-PBE calculations. The Li ions of the ground states at low compositions exclusively fill P_s sites. Many ground states are Li-vacancy orderings in super cells of the primitive cell obtained by doubling (or quadrupling in the case of $Li_{4.25}PNb_9O_{25}$) the primitive cell c axis. Orderings in each layer are shown side by side.

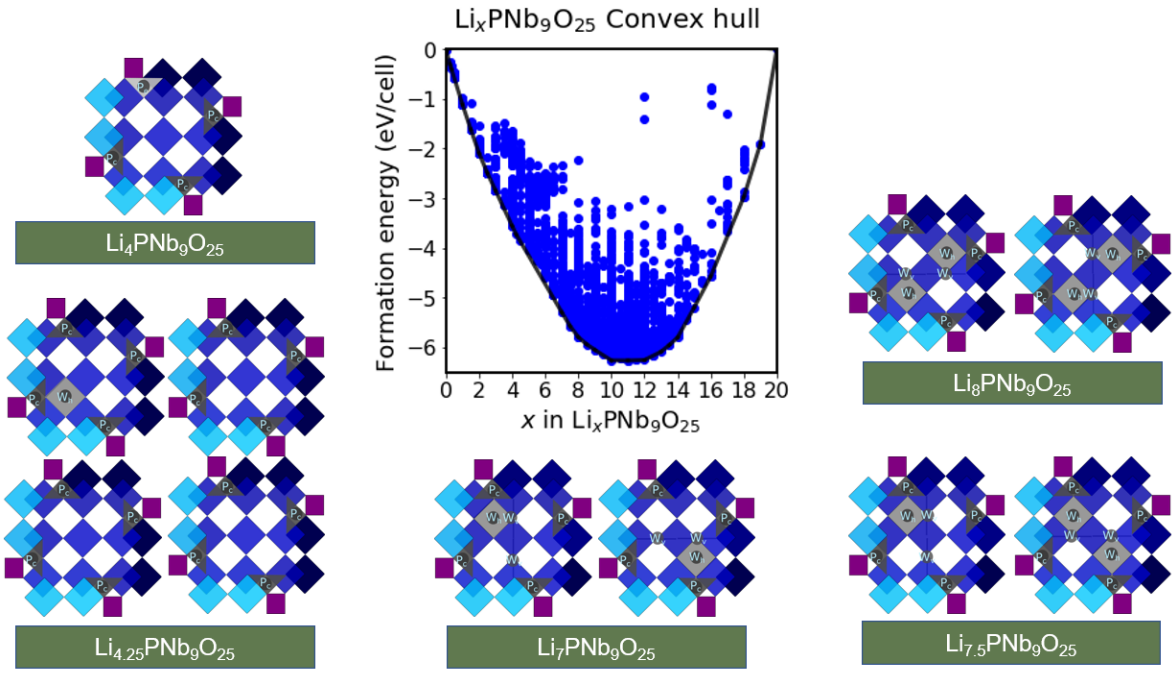

Figure 6: Formation Energies and schematics of ground state orderings of $Li_xPNb_9O_{25}$ at intermediate compositions as determined with DFT-PBE calculations. Between compositions of x=4 and x=8, Li no longer fills P_s sites, but instead fills P_c sites. The interweaved ordering over the W_v sites is stable at compositions greater than x=7.

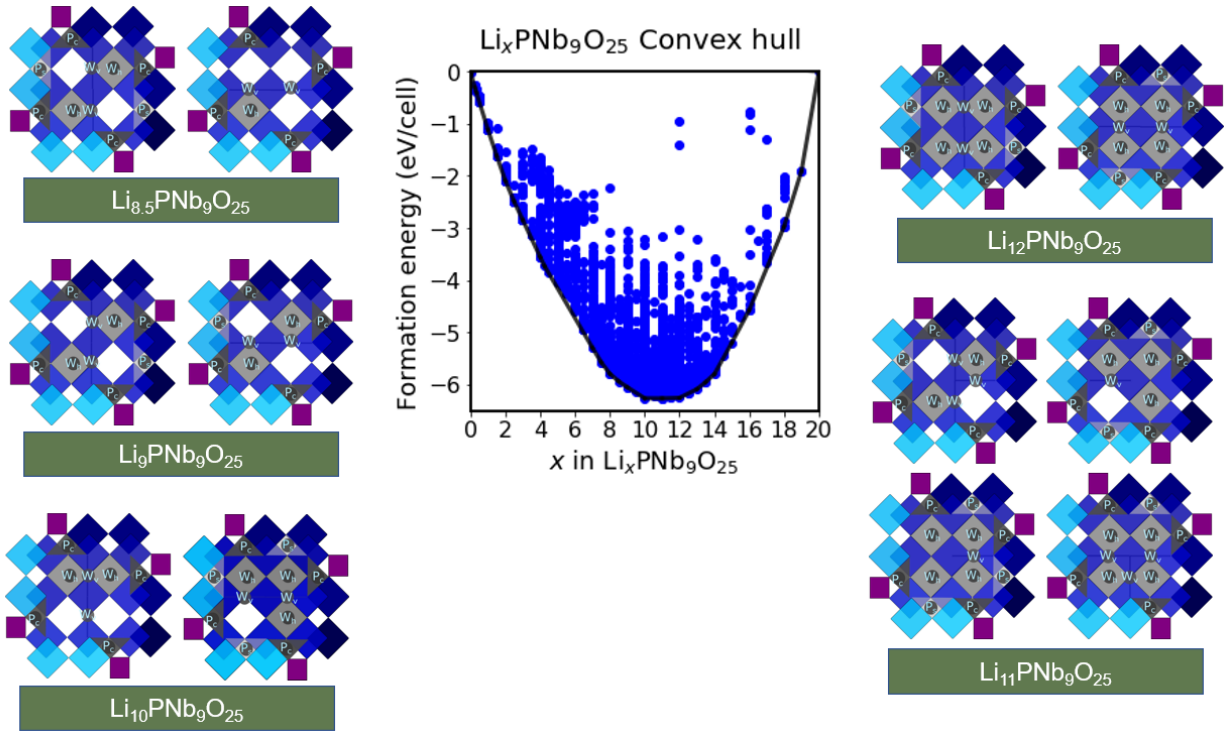

Figure 7: Formation energies and schematics of ground state orderings of $Li_xPNb_9O_{25}$ at intermediate compositions as determined with DFT-PBE calculations. Between compositions of x=8.5 and x=12, Li fills P_s sites in addition to the P_c sites and the window sites. The interweaved ordering over the W_v sites is stable in most ground states in this composition range.

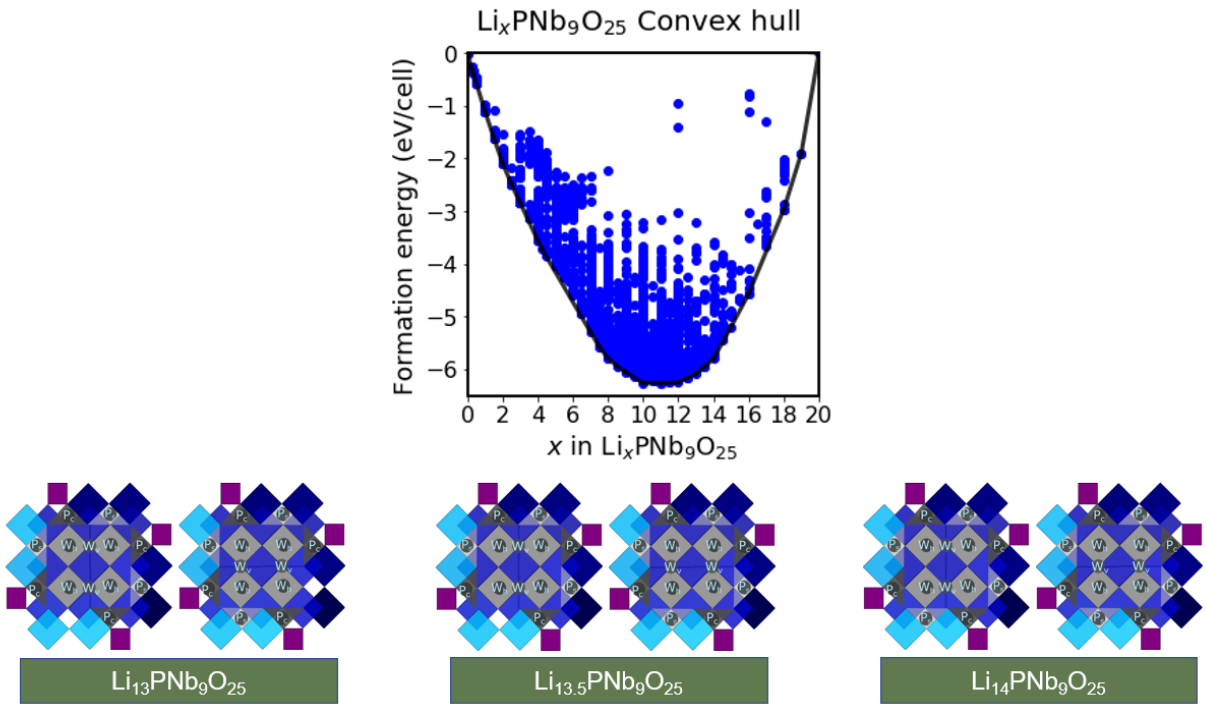

Figure 8: Formation energies and schematics of ground state orderings of $Li_xPNb_9O_{25}$ between x=13 and x=14 as determined with DFT-PBE calculations.

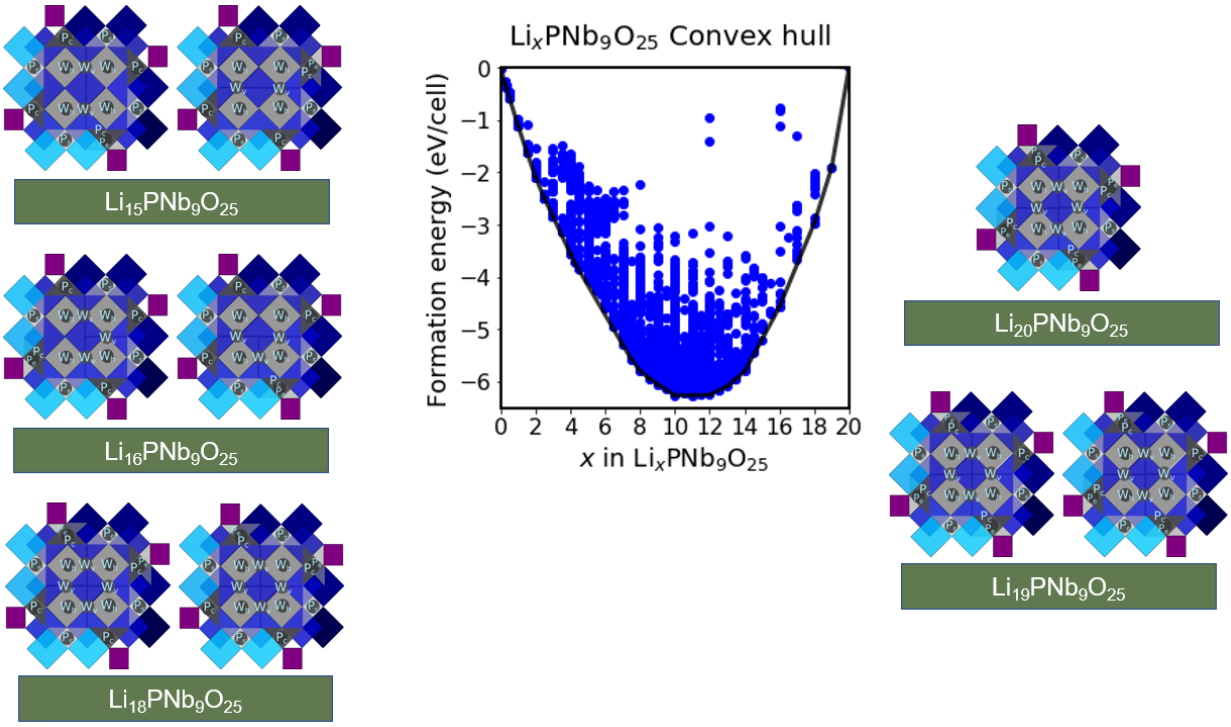

Figure 9: Formation energies and schematics of ground state orderings of LixPNb$_9$O$_{25}$ beyond x=15 as determined with DFT-PBE calculations.

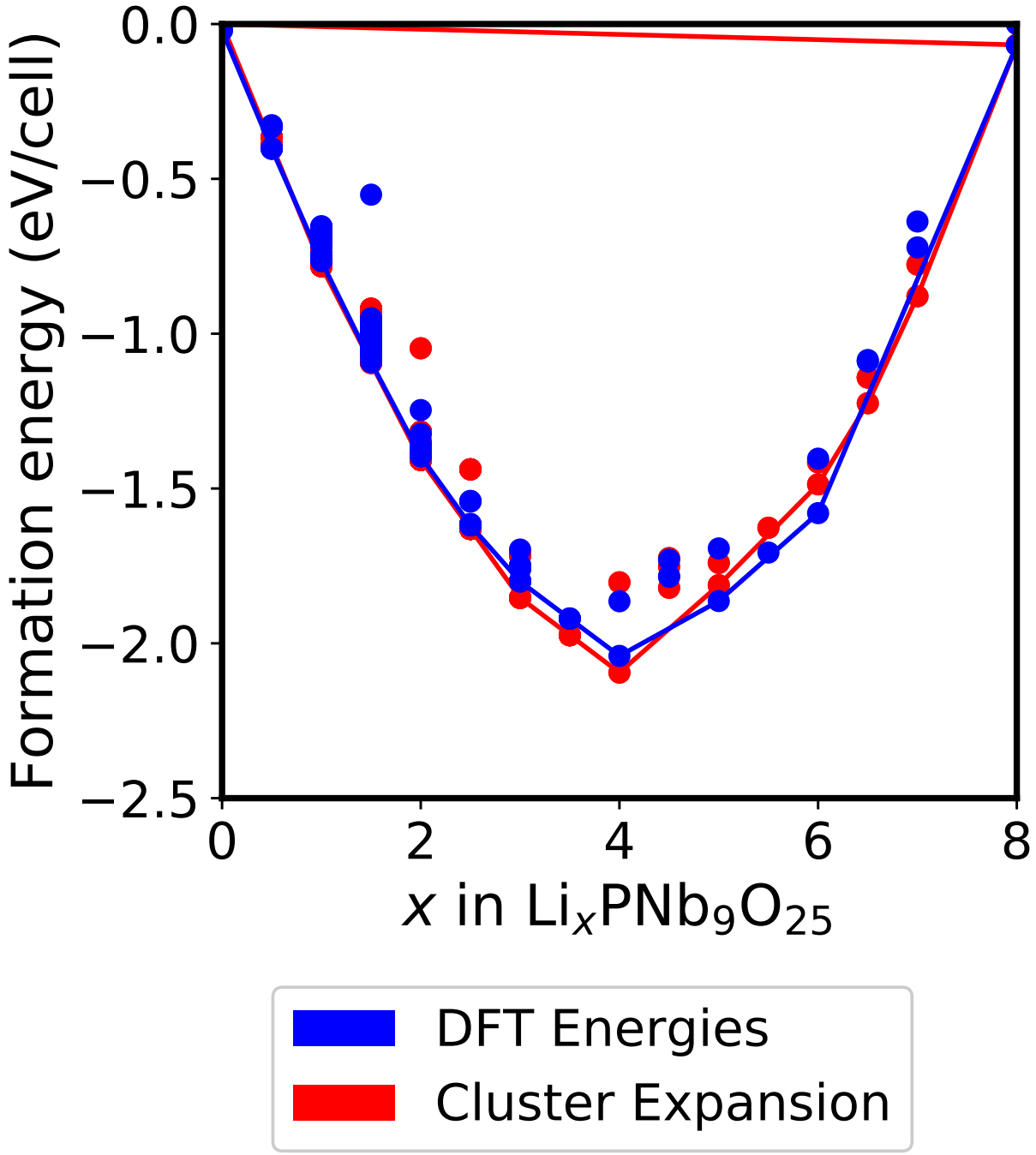

Figure 10: Comparison of formation energies as calculated with DFT-PBE and the cluster expansion at low Li concentrations. At low Li concentrations Li preferentially fills the P_e and P_s sites. The cluster expansion model for low concentrations explicitly treated the P_e and P_s sites.

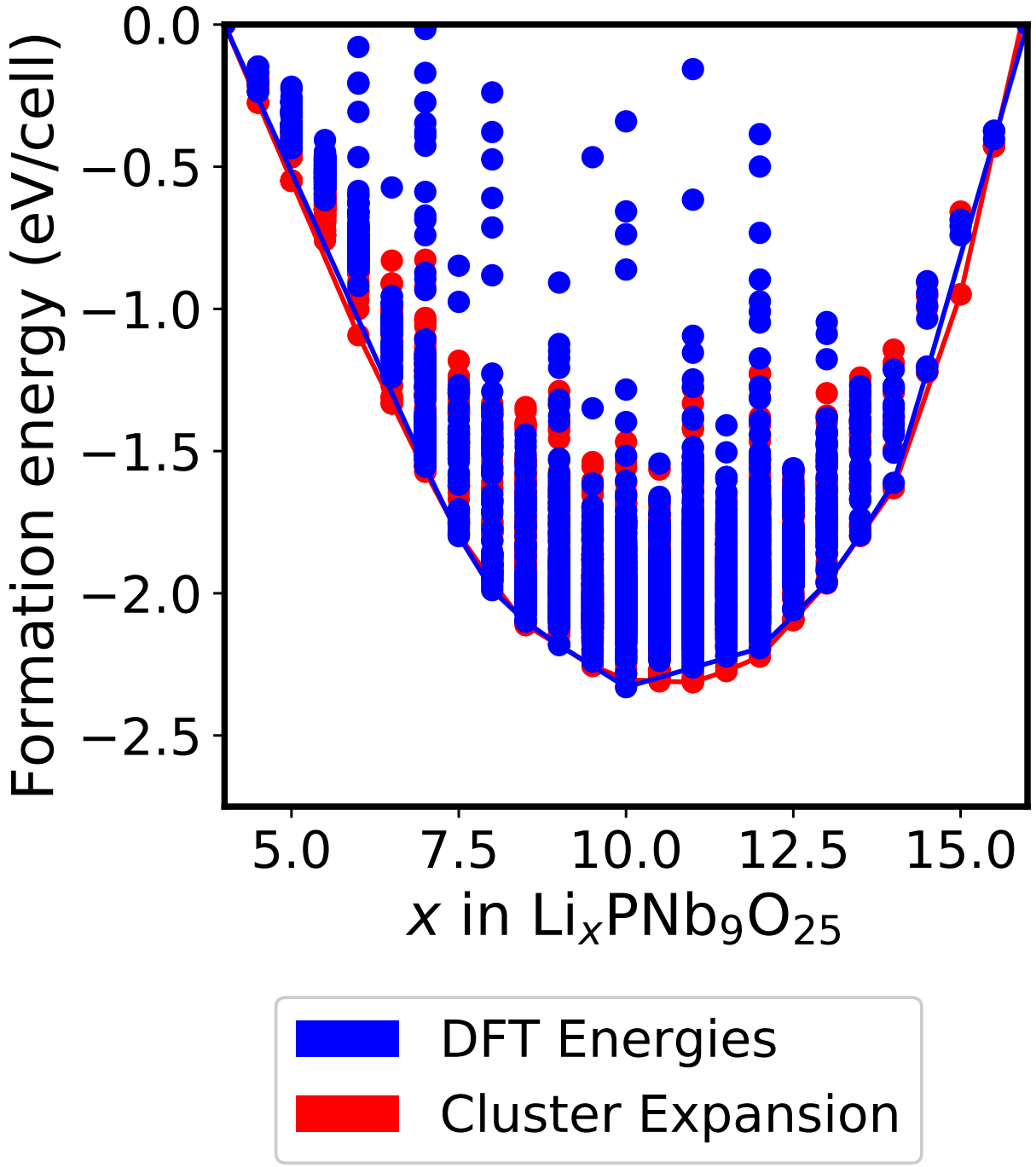

Figure 11: Comparison of formation energies as calculated with DFT-PBE and the cluster expansion at intermediate to high Li concentrations. Between x=4 and x=16 Li fills P_s, P_c, W_h and W_v sites. The cluster expansion model treats configurational degrees of freedom over the P_s, W_h and W_v sites, with the P_c sites fully filled by Li.

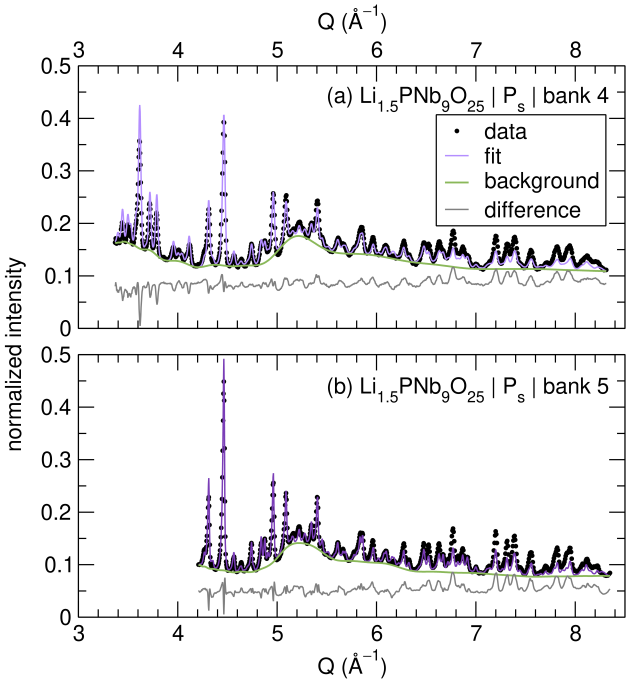

Figure 12: Neutron diffraction from NOMAD at the Spallation Neutron Source at Oak Ridge National Lab of $Li_{1.5}PNb_9O_{25}$ lithiated as a loose powder mixed with SuperP. Rietveld refinement with Li in the P_s site using (a) bank 4 and (b) bank 5, which were refined together. (c) The resulting structure determined by the refinement.

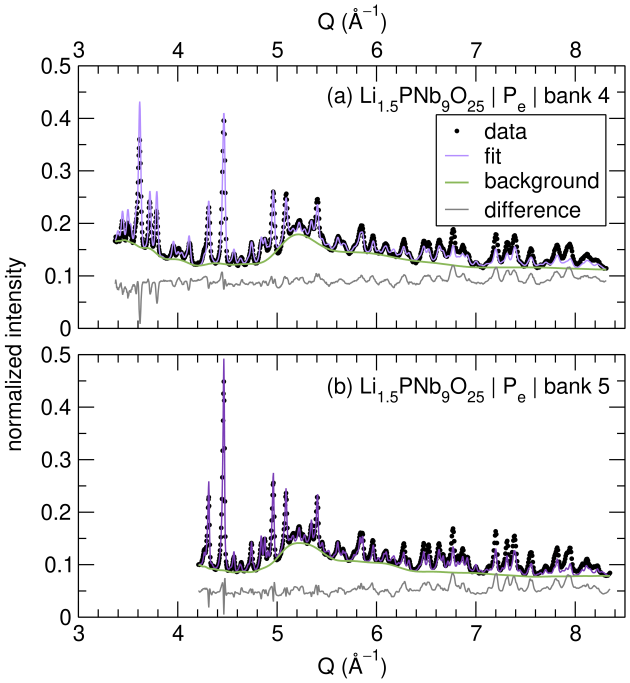

Figure 13: Neutron diffraction from NOMAD at the Spallation Neutron Source at Oak Ridge National Lab of $Li_{1.5}PNb_9O_{25}$ lithiated as a loose powder mixed with SuperP. Rietveld refinement with Li in the P_e site using (a) bank 4 and (b) bank 5, which were refined together. (c) The resulting structure determined by the refinement.

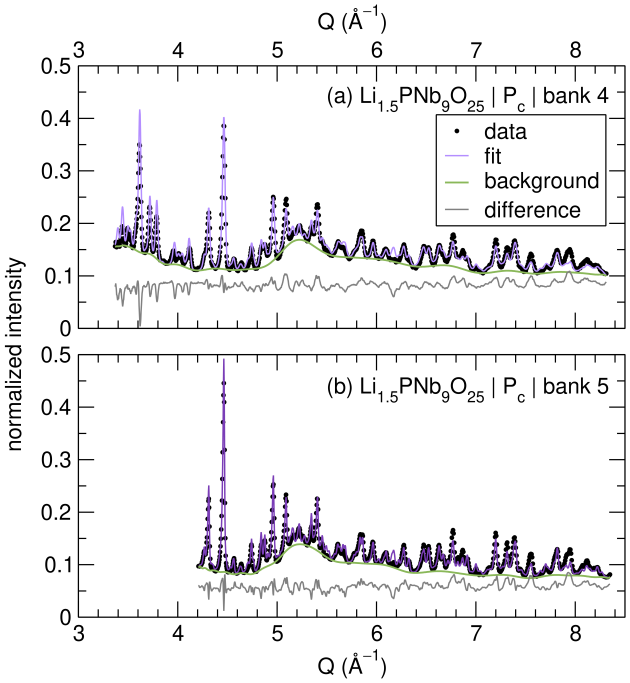

Figure 14: Neutron diffraction from NOMAD at the Spallation Neutron Source at Oak Ridge National Lab of $Li_{1.5}PNb_9O_{25}$ lithiated as a loose powder mixed with SuperP. Rietveld refinement with Li in the P_c site using (a) bank 4 and (b) bank 5, which were refined together. (c) The resulting structure determined by the refinement.

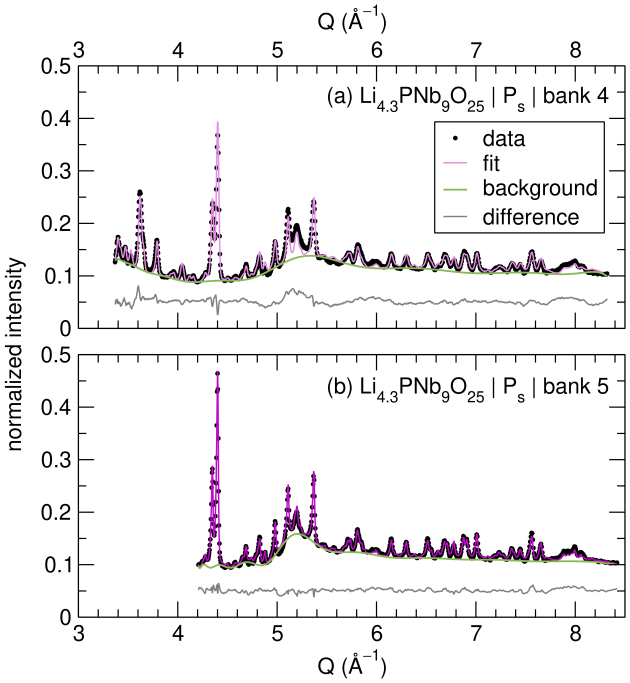

Figure 15: Neutron diffraction from NOMAD at the Spallation Neutron Source at Oak Ridge National Lab of $Li_{4.3}PNb_9O_{25}$ lithiated as a loose powder mixed with SuperP. Rietveld refinement with Li in the P_s site using (a) bank 4 and (b) bank 5, which were refined together. (c) The resulting structure determined by the refinement.

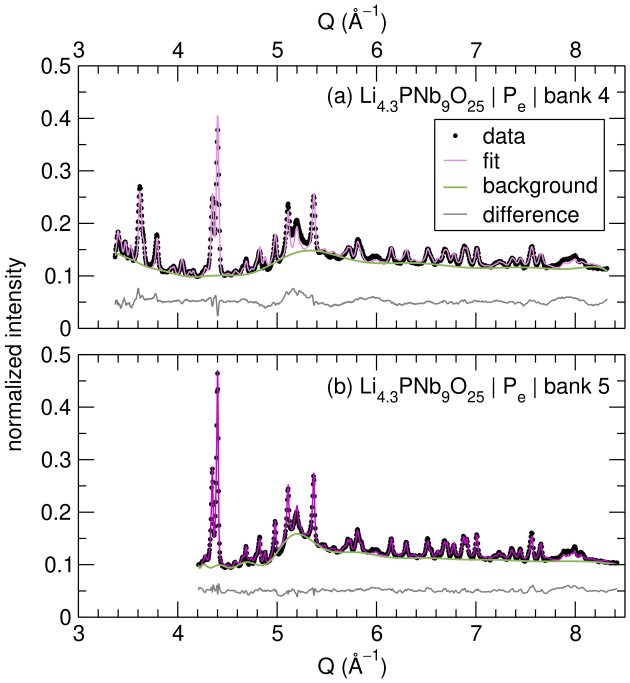

Figure 16: Neutron diffraction from NOMAD at the Spallation Neutron Source at Oak Ridge National Lab of $Li_{4.3}PNb_9O_{25}$ lithiated as a loose powder mixed with SuperP. Rietveld refinement with Li in the P_e site using (a) bank 4 and (b) bank 5, which were refined together. (c) The resulting structure determined by the refinement.

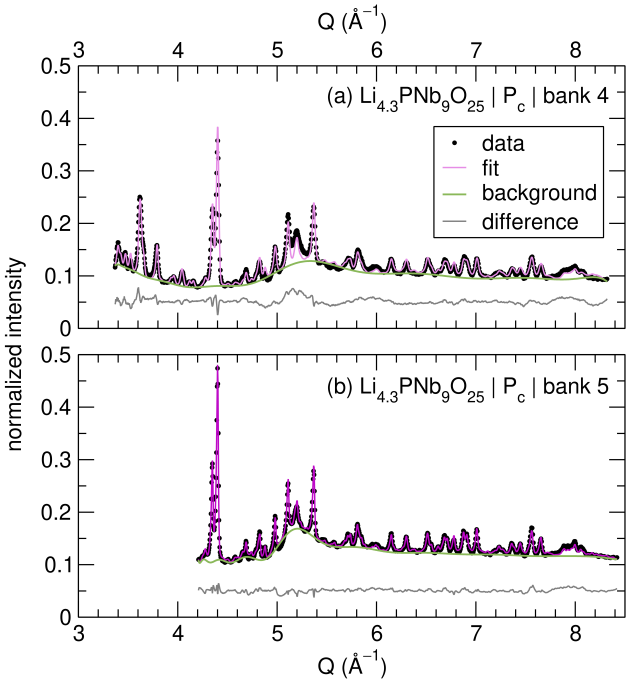

Figure 17: Neutron diffraction from NOMAD at the Spallation Neutron Source at Oak Ridge National Lab of $Li_{4.3}PNb_9O_{25}$ lithiated as a loose powder mixed with SuperP. Rietveld refinement with Li in the P_c site using (a) bank 4 and (b) bank 5, which were refined together. (c) The resulting structure determined by the refinement.

Table 1: Table of most relevant results from Rietveld refinements of 6 total configurations for $Li_{1.5}PNb_9O_{25}$ (Table 1) and $Li_{4.3}PNb_9O_{25}$ (Table 2) used to judge which Li sites are experimental candidates at each composition. The atomic positions were allowed to refine (excluding special positions), along with the thermal parameters (U_{iso}). The site occupancies were fixed according to the stoichiometry given by the galvanostatic discharge used to generate the samples.

Table 1

1.5 Li								
Li site	refined Li x	refined Li y	refined Li z	fixed Li occupancy	refined Li thermal parameter	Rwp bank 5	Rwp bank 4	candidate?
Pe (1)	0.89049	0.45654	0.5	0.375	0.11533	6.556	6.309	yes
Ps (2)	0.27367	0.2837	0	0.375	0.17465	6.921	6.58	yes
Pc (3)	-0.04517	0.32065	0.5	0.375	0.12934	5.615	6.123	borderline
Wv (4)	0.527	0.41841	1	0.375	0.28167	5.357	5.513	no
Wh (5)	0.20133	-0.07842	0	0.375	0.66996	6.022	6.759	no
none	N/A	N/A	N/A	0	N/A	5.154	5.427	N/A

represented in main text

unphysical

Table 2

4.3 Li								
Li site	refined Li x	refined Li y	refined Li z	fixed Li occupancy	refined Li thermal parameter	Rwp bank 5	Rwp bank 4	candidate?
Pe (1)	0.88804	0.5009	0.5	1	0.0592	3.507	6.024	yes
Ps (2)	0.26544	0.28004	0	1	0.0424	3.515	5.997	yes
Pc (3)	0.0253	0.34353	0.5	1	0.0164	3.458	5.939	yes
Wv (4)	0.2112	0.55176	1	1	0.9648	3.699	6.084	no
Wh (5)	0.10453	0.00635	0	1	0.17231	3.662	6.046	no
none	N/A	N/A	N/A	0	N/A	3.598	6.089	N/A

represented in main text

unphysical

The structures that most obviously did not fit the diffraction patterns, namely the two window sites (W_v, W_h), lead to Li-O bond lengths that are not physical. For the most part, the host structure remained stable in all refinements, though for $Li_{4.3}PNb_9O_{25}$, the refinement with the W_v site led to significant Nb-O bond distortion as well. U_{iso} values above 0.2 were also deemed to be unphysical. The structures represented in the main text were chosen by the results giving the most reasonable Li-O bond lengths, U_{iso} values, and lowest R_{wp} values. The other candidate structures shown in (white) are also statistically similar and are treated as candidates as well. All of the sites were tried in isolation of one another, so these results do not speak on the likelihood of any combination of sites explicitly, though likely the candidate sites do occur simultaneously within the structure.

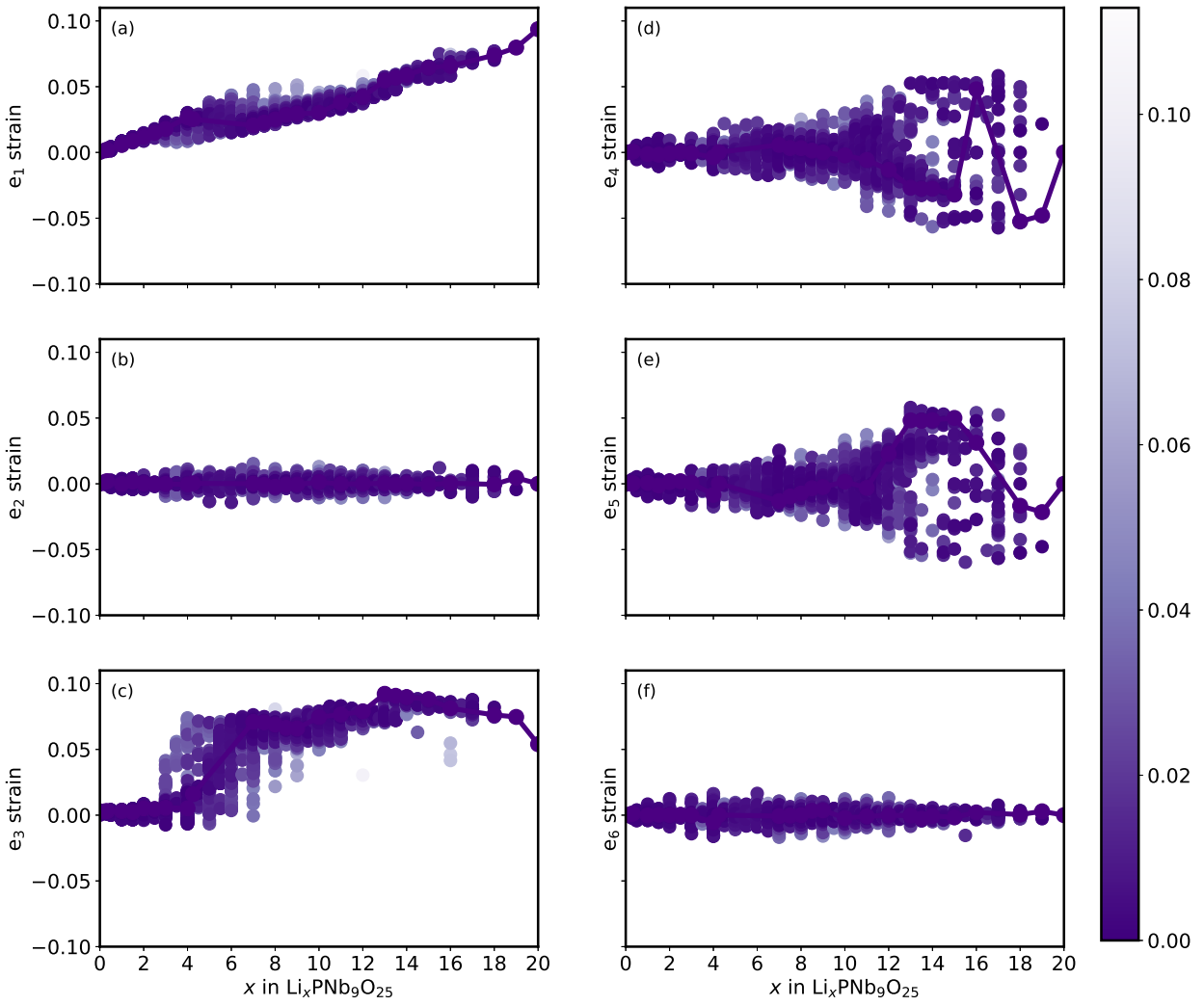

Figure 18: Distortions of the $Li_xPNb_9O_{25}$ unit cell (relative to that of PNb_9O_{25}) upon lithiation as measured with symmetry adapted strain order parameters. The formulation of the strain order parameters can be found in the text.

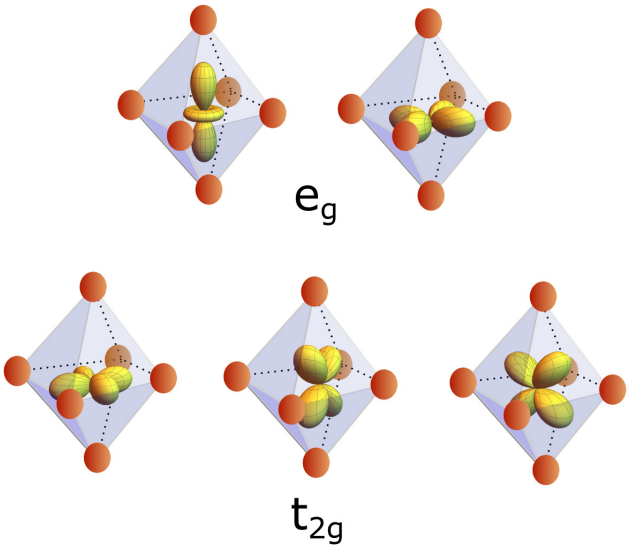

Figure 19: Illustration of the e_g and t_{2g} states on Nb of a NbO_6 octahedron.

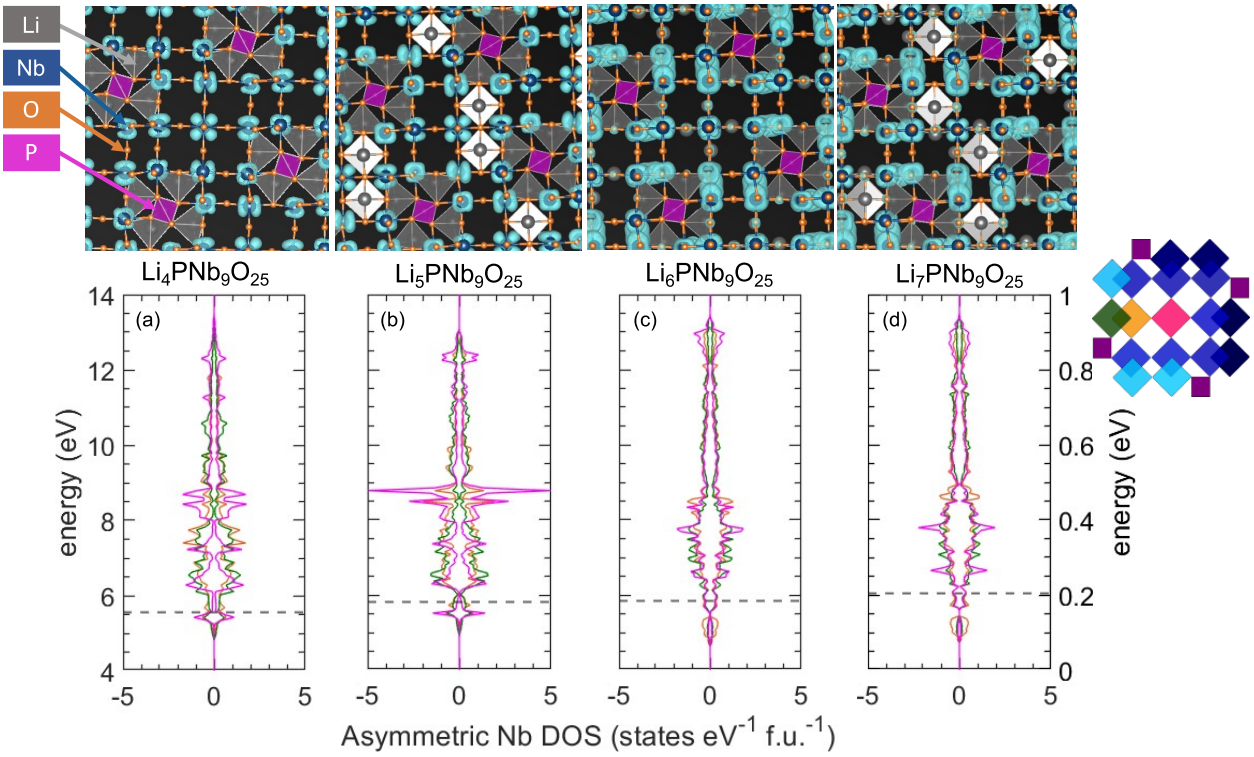

Figure 20: (a-d) Calculated charge density and density of states at x=4, 5, 6, and 7 in $Li_xPNb_9O_{25}$. An increase in the magnitude of delocalization occurs when the interweaving W_v sites are occupied